Chapter 2
Physical Processes in Lasers and VCSEL Design

Semiconductor laser physics is both a very complicated and at the same time a very exciting field. Many excellent books about the physics of semiconductor lasers and other photonic devices have been published, among other [1–4]. Physical processes taking place inside of a laser chip are of intricate nature. Optical, electrical and thermal phenomena have equal importance for the laser operation. Also mechanical phenomena, for example stress, should be considered. Moreover, these phenomena are not independent from each other but build in their strong and commonly non-linear interactions a complex picture of the physical processes inside of a device. For example current flow generates heat, temperature changes affect among other electrical resistance and refractive index of semiconductor materials, presenting photons change carrier concentrations due to absorption and so on. Many physical processes naturally arise from interactions between different fields or particles. For example generation and absorption of the light is an opto-electrical interaction phenomenon between photons and electron–hole pairs. Nonradiative recombination is an interaction process between carriers and phonons, thus an electro-thermal process. For VCSELs the interactions between various physical processes become even stronger than for edge emitting lasers because of their smaller volume, where some dimensions become comparable to the wavelength of the emitting light. For a correct understanding of the VCSEL operation optical, electrical and thermal processes inside of the laser should be considered together, including all important interactions. In Fig. 2.1 interactions between different physical phenomena inside of a VCSEL are shown.

Additionally, because in the modern semiconductor lasers active regions utilizing quantum effects, e.g. QWs or quantum dots (QDs), are implemented, the correct description of the physical processes like photon emission or absorption should be carried out using quantum mechanics. To make the picture even more complicated, time dependence could be introduced, since one is often interested in the modulation properties of lasers.

A. Mutig, *High Speed VCSELs for Optical Interconnects*, Springer Theses,
DOI: 10.1007/978-3-642-16570-2_2, © Springer-Verlag Berlin Heidelberg 2011

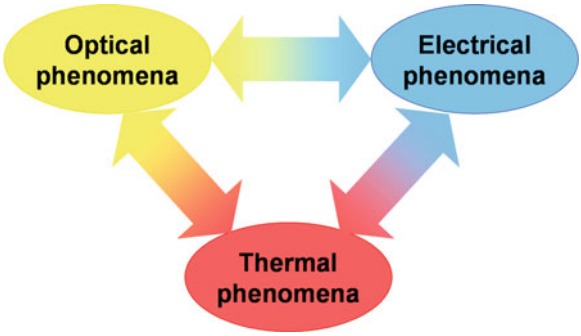

Fig. 2.1 Optical, electrical and thermal phenomena in a semiconductor laser and their interaction

Ideally, a complete opto-electro-thermal three-dimensional model with quantum mechanical description of the active region should be used in order to get the complete picture of the physical processes inside of a VCSEL. In fact such advanced models, dealing with complete or partially coupled opto-electro-thermal phenomena, exist both commercially [5–8] and also in the research groups [9]. Unfortunately their application is very recourse-consuming and usually requires powerful super-computers equipped with parallel processors and enormous amount of memory. In addition, to operate such software efficiently is mostly time-consuming and requires a lot of experience in complicated theoretical simulations of semiconductor devices.

Fortunately, in order to understand basic principles of VCSEL operation, to be able to analyse measurement results efficiently and to design new devices correctly, the application of the complex three-dimensional coupled opto-thermo-electrical models is not implicit necessary. Having a deeper understanding of the physical processes inside of the laser and knowing the basic semiconductor laser theory enable to solve the tasks, that are important for VCSEL designing and analysis, using simpler models. In this case optical, electrical and thermal properties of a VCSEL could be treated separately and all necessary interactions between these phenomena could be considered manually.

In this work optical, electrical and thermal properties of VCSELs have been investigated using decoupled models. Physical parameters, which have been extracted from these individual models, have been then used for device designing and analysis under application of the rate equation model for photon and carrier dynamics.

2.1 Optical Properties

The main purpose of any laser is to generate light, and light is an electro-magnetic wave and thus an optical phenomenon. That is why the optical properties of any laser are playing an important role in the laser physics. In many cases one-dimensional treatment of the optical fields is sufficient. From the other side, many

important laser characteristics, especially in the case of VCSELs, could not be calculated from one-dimensional models, making three-dimensional simulations necessary. The presence of the rotation symmetry in VCSELs simplifies the situation, thus effectively two-dimensional optical simulations could be sufficient.

A commonly used model for one-dimensional calculations is the transmission or transfer matrix method [2], which is very fast and easy to use. This model enables easily to calculate among other reflectivity spectra of the multilayered distributed Bragg reflectors (DBR), which act as top and bottom mirrors, longitudinal standing wave pattern inside of the VCSEL cavity and the cavity dip position. This basic information is inalienable for the correct VCSEL designing. Nevertheless for a deeper understanding of the optical laser properties, especially for oxide-confined VCSELs, three-dimensional field distributions for the ground and also higher order lasing modes as well as important mode parameters, e.g. mode volume and optical confinement factor, should be accessible. Such kind of calculations could be carried out only by three-dimensional or, in the case of the presence of rotation symmetry, also by two-dimensional models.

Several models for two-dimensional and three-dimensional simulations exist and can be divided into scalar, vectorial and hybrid models. Scalar models solve scalar Helmholtz equation and are commonly fast, but not very accurate in handling the higher order lasing modes or devices with smaller dimensions. Vectorial models solve Maxwell's equations exactly, without any approximations. These models are slower than scalar methods but can handle every optical field, including also those with a relatively large transverse wavevector component, like in the case of higher order modes or smaller devices, accurately. Hybrid models are in between and apply both scalar and vectorial approaches to deal with different optical subproblems.

Commonly used scalar models are the effective index model [10], the effective frequency method [11] and the effective index model with eigenmodes [12]. From the vectorial models the Green's function model [13], the full-vector weighted index method [14] and the eigenmode expansion with perfectly matched layers (PML) [15, 16], are commonly used. An overview and a comparison of different optical models could be found in [17].

In this work both the one-dimensional transfer matrix method and the three-dimensional eigenmode expansion technique with PMLs, both implemented in the free CAMFR software [18] were applied.

2.1.1 Transfer Matrix Method and 1D Simulations

The general equations describing electro-magnetic fields are the Maxwell's equations [1], which relate electric field $\vec{E}$, magnetic field $\vec{H}$, electric displacement flux density $\vec{D}$ and magnetic flux density $\vec{B}$ to the charge density ρ and the current density $\vec{J}$ (2.1.1–2.1.4).

$$\vec{\nabla} \times \vec{E} = -\frac{\partial}{\partial t}\vec{B} \tag{2.1.1}$$

$$\vec{\nabla} \times \vec{H} = \vec{J} + \frac{\partial}{\partial t}\vec{D} \tag{2.1.2}$$

$$\vec{\nabla} \cdot \vec{D} = \rho \tag{2.1.3}$$

$$\vec{\nabla} \cdot \vec{B} = 0. \tag{2.1.4}$$

Thereby the two source terms, the charge density and the current density, are not independent but related by the continuity equation (2.1.5).

$$\vec{\nabla} \cdot \vec{J} + \frac{\partial}{\partial t}\rho = 0 \tag{2.1.5}$$

The quantities $\vec{E}$, $\vec{H}$, $\vec{D}$ and $\vec{D}$ are also not independent but related by the constitutive relations, that involve the properties of the medium:

$$\vec{D} = \varepsilon \cdot \vec{E}, \tag{2.1.6}$$

$$\vec{B} = \mu \cdot \vec{H}, \tag{2.1.7}$$

where ε is in a common case the permittivity tensor and μ is the permeability tensor. For an isotropic media ε and μ are scalars.

For time-harmonic fields it is common to apply the so called phasor notation, where the harmonic time dependence is represented by the complex exponents of the form $e^{j\omega t}$ and j is the imaginary unit. The real time-dependent fields can be then extracted from the complex phasors using Eqs. 2.1.8 and 2.1.9:

$$\vec{E}(\vec{r}, t) = \mathrm{Re}\left\{\vec{E}(\vec{r}, \omega) \cdot e^{j\omega t}\right\}, \tag{2.1.8}$$

$$\vec{H}(\vec{r}, t) = \mathrm{Re}\left\{\vec{H}(\vec{r}, \omega) \cdot e^{j\omega t}\right\}. \tag{2.1.9}$$

Here $\vec{E}(\vec{r}, t)$ and $\vec{H}(\vec{r}, t)$ are the real electric and magnetic fields and $\vec{E}(\vec{r}, \omega)$ and $\vec{H}(\vec{r}, \omega)$ the complex phasors, which are not time-dependent. In the further equations we will use the symbols $\vec{E}$, $\vec{H}$ etc. for phasors, if nothing special is noted. All other quantities could be easily converted to the phasors and back using the same rules.

The phasor notation simplifies mathematical calculations and representation of simulation results. Maxwell equations for a homogeneous isotropic medium without any charges and current flow ($\vec{J} = 0$ and $\rho = 0$) could be then written down using phasors and substituting $\vec{D}$ and $\vec{B}$ from Eqs. 2.1.6 and 2.1.7 as follows:

$$\vec{\nabla} \times \vec{E} = -j\omega\mu\vec{H}, \tag{2.1.10}$$

$$\vec{\nabla} \times \vec{H} = \vec{J} + j\omega\varepsilon\vec{E}, \tag{2.1.11}$$

$$\vec{\nabla} \cdot \vec{D} = \rho, \tag{2.1.12}$$

$$\vec{\nabla} \cdot \vec{B} = 0. \tag{2.1.13}$$

Equations 2.1.6 and 2.1.7 stay unchanged.

The solutions of the Maxwell's equation in an isotropic dielectric medium are plane waves of the form

$$\vec{E}_f = \vec{e}E_f e^{-\beta z}, \tag{2.1.14}$$

$$\vec{E}_b = \vec{e}E_b e^{\beta z}, \tag{2.1.15}$$

for the forward propagating wave $\vec{E}_f$ and the backwards propagating wave $\vec{E}_b$. The unit vector $\vec{e}$ determines the polarization of the light. The propagation direction is parallel to the z-axis. The quantity β is the propagation constant and for the plane wave in an isotropic dielectric medium is determined by the refractive index of the medium n:

$$\beta = \omega n/c. \tag{2.1.16}$$

Transfer matrix formalism handles plane waves and use the fact that each interface between two isotropic dielectric media as well as each layer could be represented by 2×2 matrices, which are called transmission or transfer matrices T. Each transmission matrix relates forward and backward propagating field amplitudes $E_{1,f}$ and $E_{1,b}$ on one side of the interface or layer with the forward and backward propagating fields $E_{2,f}$ and $E_{2,b}$ on the other side:

$$\begin{pmatrix} E_{1,f} \\ E_{1,b} \end{pmatrix} = \begin{pmatrix} T_{11} & T_{12} \\ T_{21} & T_{22} \end{pmatrix} \begin{pmatrix} E_{2,f} \\ E_{2,b} \end{pmatrix} = T \begin{pmatrix} E_{2,f} \\ E_{2,b} \end{pmatrix}. \tag{2.1.17}$$

The great advantage comes into play by using the transfer matrix method for multilayered structures. For the complete stack of layers one can simple multiply the corresponding T_i matrices of each individual layer and interface and so get the T_S matrix for the whole stack:

$$T_S = T_1 \cdot T_2 \cdot \cdots \cdot T_i \cdot \cdots \cdot T_{N-1} \cdot T_N, \tag{2.1.18}$$

where N is the total number of the layers and interfaces. This idea together with the definitions of the forward and backward directions is illustrated in Fig. 2.2.

The transmission matrices can be easily calculated for plane waves and for the case of the normal incidence for an interface between two media with refractive indices $n_1$and n_2, and also for a layer with the thickness L according to Eqs. 2.1.19 and 2.1.20, respectively,

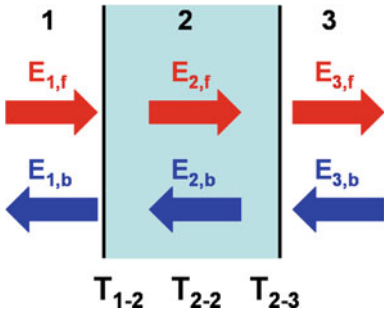

Fig. 2.2 Transmission matrices for a stack consisting of three media 1, 2 and 3 and two interfaces

$$T_{\text{interface}} = \frac{1}{t_{12}}\begin{pmatrix} 1 & r_{12} \\ r_{12} & 1 \end{pmatrix}, \tag{2.1.19}$$

$$T_{\text{layer}} = \begin{pmatrix} e^{-j\beta L} & 0 \\ 0 & e^{j\beta L} \end{pmatrix}, \tag{2.1.20}$$

with r_{12} and t_{12} given by the following equations:

$$r_{12} = \frac{n_1 - n_2}{n_1 + n_2}, \tag{2.1.21}$$

$$t_{12} = \frac{2n_1}{n_1 + n_2}. \tag{2.1.22}$$

Transfer matrix method is very simple to use and do not require noticeable computational power. Using this formalism in the present work 1D-simulations for DBR reflectivity spectra, cavity dip position and field distribution inside of the cavity were carried out. In the following a short outline of each of these three tasks with exemplary simulation results used for VCSEL designing will be given.

One of the first tasks while designing a VCSEL is to decide, how many DBR pairs for the top and the bottom mirror should be grown. This determines the reflectivity of the both mirrors. Figure 2.3a shows the reflectivity and phase spectra for the top $Al_{0.12}Ga_{0.88}As/Al_{0.90}Ga_{0.10}As$ DBR with 23.5 pairs used in the 980 nm QW-VCSELs. The simulation includes two 30 nm thick $Al_{0.98}Ga_{0.02}As$ layers for the later wet oxidation, in the first DBR pair closest to the cavity and just below it. To minimize electrical resistance 20 nm thick linear gradings were applied and also token into consideration for the simulations.

From Fig. 2.3a can be obtained that the maximum reflectivity and also the zero phase appear at the desired wavelength of 980 nm. Figure 2.3b demonstrates dependence of the peak reflectivity on the number of the DBR pairs. Adding additional two pairs to 21.5 pairs increase the reflectivity at 980 nm from 0.9960 up to 0.9977. For VCSELs reflectivity of the mirrors should be designed with a

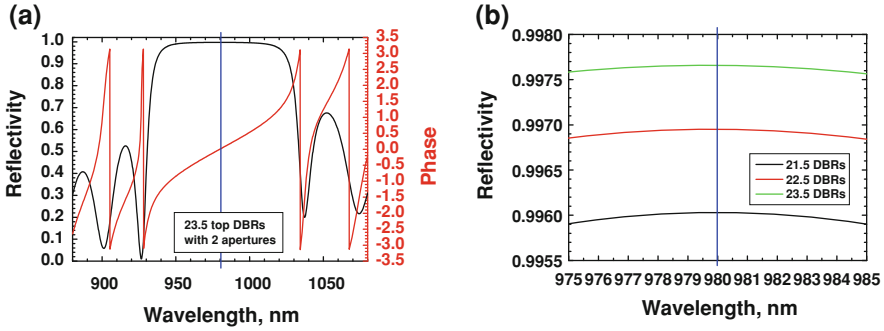

Fig. 2.3 Reflectivity and phase as a function of the wavelength of an $Al_{0.12}Ga_{0.88}As/Al_{0.90}Ga_{0.10}As$ DBR with 23.5 DBR pairs including two $Al_{0.98}Ga_{0.02}As$ layers for the later oxidation (**a**) and reflectivity as a function of the number of the DBR pairs (**b**)

very high precision, so that four numbers after the decimal point should be considered. According to the well known equation [1, 2]

$$\Gamma g_{\text{thr}} = \alpha_i + \frac{1}{2L}\ln\left(\frac{1}{R_1 R_2}\right) = \alpha_i + \alpha_m = \alpha_{\text{tot}}, \tag{2.1.23}$$

where Γ is the optical confinement factor, g_{th} the threshold gain, α_i the intrinsic cavity loss, α_m the mirror loss, α_{tot} the total loss, R_1 and R_2 the power reflection coefficients of the top and bottom mirrors and L the effective cavity length, the reflectivity of each mirror directly affects the threshold gain and thus the threshold current. Reflectivities in the range of 0.997–0.998 for the top mirror and close to 0.9998–0.9999 for the bottom mirror were used for all structures investigated in this work. For the 980 SML-VCSELs 20.5 periods of the $GaAs/Al_{0.90}GaAs$ DBRs for the top and 32.5 periods for the bottom mirror with 10 nm thick linear gradings were used. For the 980 nm QW-VCSELs 23.5 and 37.5 $Al_{0.12}Ga_{0.88}As/Al_{0.90}Ga_{0.10}As$ DBR pairs for the top and bottom mirrors respectively were grown. For the 850 nm QW-VCSELs these were 22.5 and 35 $Al_{0.15}Ga_{0.85}As/Al_{0.90}Ga_{0.10}$ DBR pairs respectively. In the last two structures the thickness of the linear gradings was 20 nm.

The second important task for a proper VCSEL design is to match the cavity wavelength to the desired value. For the VCSEL fabricated in this work these were 850 and 980 nm. For this purpose the position of the cavity dip was calculated with the transfer matrix method. Therefore reflection from the complete VCSEL structure was simulated. If necessary, the thickness of the cavity should be adjusted in order to match the dip position to the desired wavelength. Figure 2.4 shows the calculated cavity dip positions for the 850 nm QW-VCSELs and 980 nm QW-VCSELs. Both dips match the desired wavelengths sufficiently precise.

Finally, the active medium should be placed on the right place in the field intensity anti-node in order to increase the interaction of the active material with

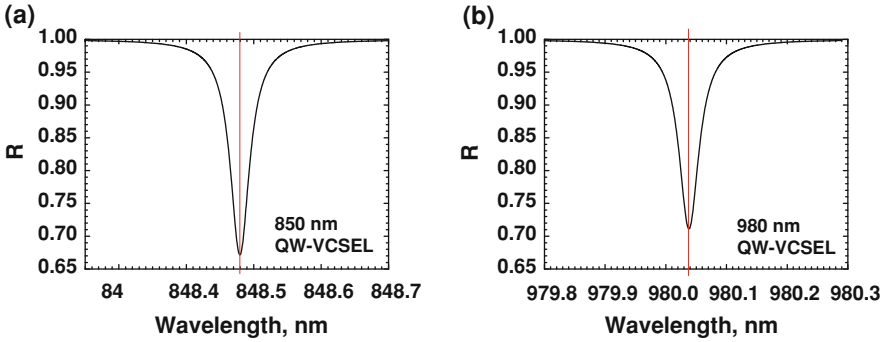

Fig. 2.4 Cavity dip position for the 850 nm QW-VCSEL (**a**) and for the 980 nm QW-VCSEL (**b**)

the optical field. For this purpose standing wave pattern of the ground mode was calculated and investigated. Calculated electrical field magnitudes together with the refractive index profiles inside of the cavity for the 850 nm QW-VCSEL, 980 nm QW-VCSEL and 980 nm SML-VCSEL are shown in Fig. 2.5a–c respectively. The growth direction on the pictures is from the right to the left and at the zero position is the air-semiconductor interface. A zoomed view of the cavity for the 850 nm QW-VCSEL and 980 nm QW-VCSEL is shown in the Fig. 2.6a, b, respectively. From both figures can be obtained that the number of the active layers is odd and the middle active layer is located exactly in the anti-node of the field intensity. The remaining active layers are placed symmetrically to the middle active layer with the possible smallest distance in order to optimize the overlap with the optical field.

As one can see, the transfer matrix method is a simple but at the same time powerful tool to solve basic important tasks for the optical VCSEL designing. Its application is very time-saving and does not require many resources. The simulation time for one calculation is commonly only few seconds, so that many calculations could be carried out within a very short time slot.

In spite of all advantages of the transfer matrix formalism, this method remains limited to one-dimensional problems and plane waves and cannot give a deeper understanding of the optical processes inside of a complex three-dimensional structure like oxide-confined VCSELs, where some dimensions become comparable to the wavelength of the emitting light. Using transfer matrix no three-dimensional field distributions and no corresponding optical parameters, e.g. three-dimensional confinement factor, mode volume etc., can be calculated. There is no direct possibility to handle higher order lasing modes. However, understanding of these phenomena and having access to the three-dimensional properties not only of the ground mode, but also of the higher order modes, is an indispensable prerequisite for a good understanding of the physical processes inside of the laser. For this purpose models, which are able to handle three-dimensional problems, should be applied. In this work the fully-vectorial eigenmode expansion technique handling two-dimensional structures was used, which

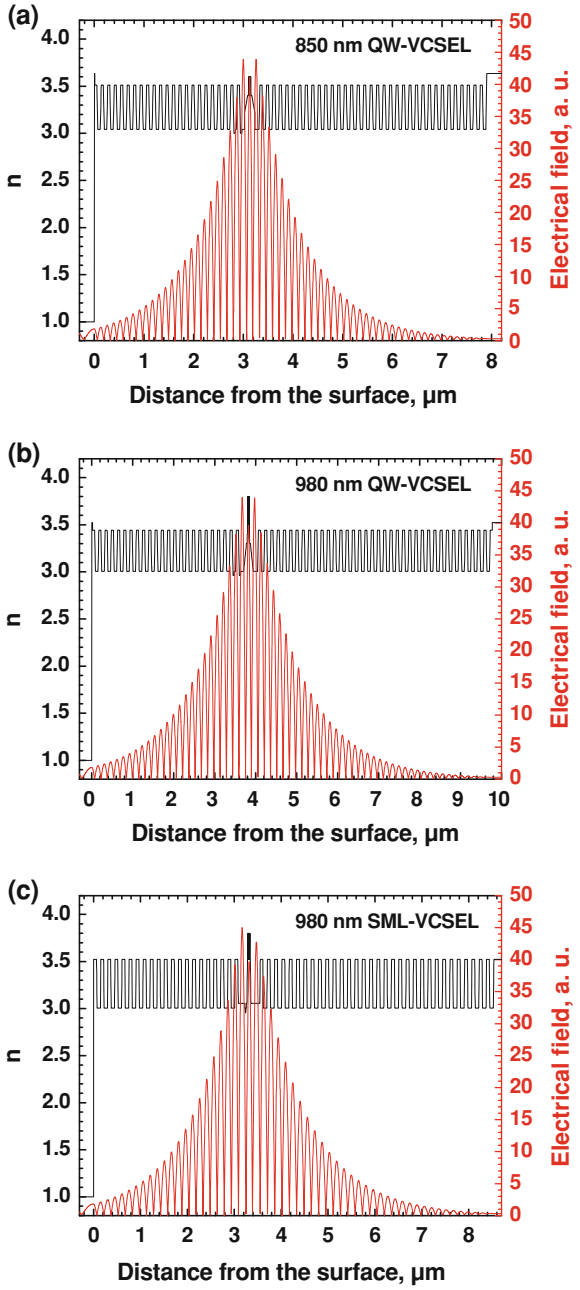

Fig. 2.5 Refractive index profile and electrical field distribution inside of the cavity for the 850 nm QW-VCSEL (**a**), 980 nm QW-VCSEL (**b**) and 980 nm SML-VCSEL (**c**). At zero position is the air–semiconductor interface

could deliver three-dimensional results because of the cylindrical symmetry of the VCSEL structures. This model and the obtained simulation results will be presented in the following sections of this chapter.

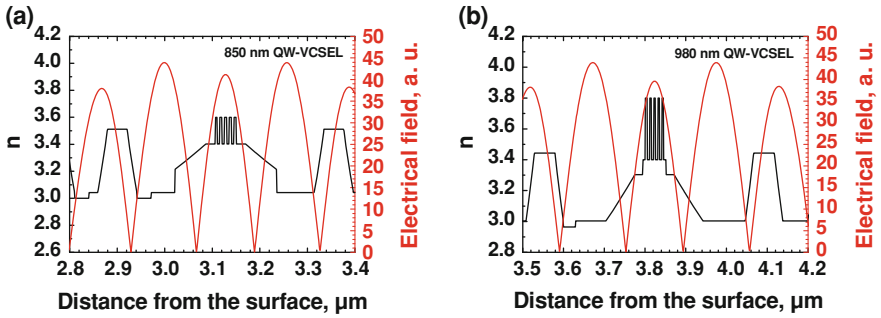

Fig. 2.6 Zoomed view of the refractive index profile and the electrical field distribution inside of the cavity for the 850 nm QW-VCSEL (**a**) and 980 QW-VCSEL (**b**)

2.1.2 Eigenmode Expansion Technique for 3D VCSEL Modeling

Most exact models apply some form of spatial discretisation in order to handle three-dimensional problems. For example for models based on finite elements [19] and finite-difference time-domain (FDTD) methods [20] some kind of grid should be generated and overlays the structure to be modeled. Then in each cell the Maxwell's equations should be solved and the found solutions should be matched to each other at each interface and also to the boundaries. This form of the spatial discretisation is very time- and resource-consuming, since large number of unknowns is generated. Simulations based on such methods require powerful computers and could take many hours or even days.

However, most real VCSEL structures do not have an arbitrary refractive index profile and in fact consist on many layers, but in each of these layers the refractive index is constant. Thus one does not need a full discretisation, and dividing of the VCSEL structure into regions with constant refractive indices, together with taking advantage of the cylindrical symmetry of the VCSEL, is sufficient for a fully three-dimensional optical simulation. Eigenmode expansion technique does exact this. The principle of the spatial discretisation used in the eigenmode expansion method compared to a grid commonly used in other models is schematically shown in Fig. 2.7.

In a z-invariant medium in cylindrical coordinates (Fig. 2.8) one can set the dependence of the electric and magnetic field on the z-coordinate to be harmonic [16]:

$$\vec{E}(\vec{r}) = \left(E_r(r,\phi)\cdot\vec{e}_r + E_\phi(r,\phi)\cdot\vec{e}_\phi + E_z(r,\phi)\cdot\vec{e}_z\right)\cdot e^{-j\beta z}, \tag{2.1.24}$$

$$\vec{H}(\vec{r}) = \left(H_r(r,\phi)\cdot\vec{e}_r + H_\phi(r,\phi)\cdot\vec{e}_\phi + H_z(r,\phi)\cdot\vec{e}_z\right)\cdot e^{-j\beta z}, \tag{2.1.25}$$

with reduced field components E_r, E_ϕ, E_z for the electric and H_r, H_ϕ, H_z for the magnetic field, which depend only on two coordinates: r and ϕ.

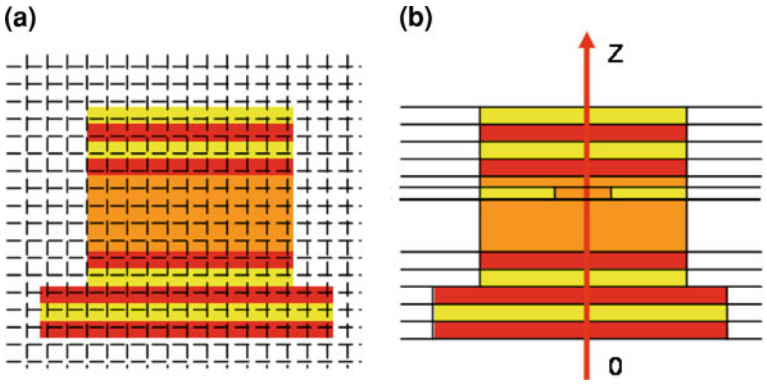

Fig. 2.7 Spatial discretisation with a grid (**a**) and in the eigenmode expansion method (**b**)

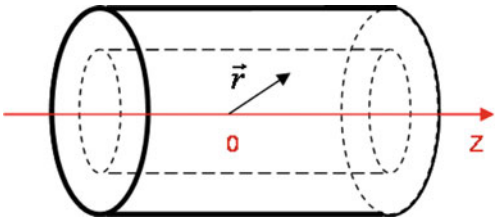

Fig. 2.8 A z-invariant medium and cylindrical coordinate system

Here β is again the propagation constant and is at the beginning not fixed. With the ansatz (2.1.24) and (2.1.25) following equations for the reduced field components could be derived from the Maxwell's equations (2.1.10–2.1.13) in cylindrical coordinates in absence of electrical charges and currents:

$$\frac{\partial^2 E_z}{\partial r^2} + \frac{1}{r}\frac{\partial E_z}{\partial r} + \frac{1}{r^2}\frac{\partial^2 E_z}{\partial \phi^2} + q^2 E_z = 0, \tag{2.1.26}$$

$$\frac{\partial^2 H_z}{\partial r^2} + \frac{1}{r}\frac{\partial H_z}{\partial r} + \frac{1}{r^2}\frac{\partial^2 H_z}{\partial \phi^2} + q^2 H_z = 0 \tag{2.1.27}$$

for the z-components of the electric and magnetic field and

$$E_r = -\frac{j}{q^2}\left(\beta\frac{z}{\partial r} + \frac{\omega\mu}{r}\frac{\partial H_z}{\partial \phi}\right), \tag{2.1.28}$$

$$E_\phi = -\frac{j}{q^2}\left(\frac{\beta}{r}\frac{\partial E_z}{\partial \phi} - \omega\mu\frac{\partial H_z}{\partial r}\right), \tag{2.1.29}$$

$$H_r = -\frac{j}{q^2}\left(\beta\frac{z}{\partial r} - \frac{\omega\varepsilon}{r}\frac{\partial E_z}{\partial \phi}\right), \tag{2.1.30}$$

$$H_\phi = -\frac{j}{q^2}\left(\frac{\beta}{r}\frac{\partial H_z}{\partial \phi} + \omega\varepsilon\frac{\partial E_z}{\partial r}\right) \tag{2.1.31}$$

for the r- and ϕ-components. Hereby is q defined as follows:

$$q = \sqrt{k^2 - \beta^2}, \tag{2.1.32}$$

with k equal to

$$k = \omega\sqrt{\mu\varepsilon}. \tag{2.1.33}$$

One can see from Eqs. 2.1.26 and 2.1.27 that the z-components of the field are decoupled from the r- and ϕ-components. Once one have solved for the z-components one can immediately solve Eqs. 2.1.28–2.1.31 for the r- and ϕ-components and thus get complete fields.

One can make several assumptions regarding the electric and magnetic fields in order to simplify the mathematical procedures and thus get different types of solutions. If one assumes that the z-components of both electric and magnetic fields are equal to zero, the so called transverse electric (TE) and transverse magnetic (TM) modes will be the solutions of (2.1.26–2.1.31). In a common case, where all components of both fields are assumed to be present, the so called hybrid modes (HE and EH) are the desired solutions. For an overview about mode classification in circular cylindrical structures one can refer to [21–23].

For the cylindrical symmetry the ϕ-dependence of the z-components of the electric and magnetic field can be assumed to be as follows:

$$E_z(r,\phi) = A \cdot F_v(r) \cdot e^{jv\phi}, \tag{2.1.34}$$

$$H_z(r,\phi) = B \cdot F_v(r) \cdot e^{jv\phi}, \tag{2.1.35}$$

where A and B are constants, v is a whole number (0, 1, 2, …) and the function $F_v(r)$ depends only on the r coordinate and also parametrically on v. With this ansatz one gets the equation for the function $F_v(r)$ from (2.1.26) and (2.1.27):

$$\frac{\partial^2 F_v}{\partial r^2} + \frac{1}{r}\frac{\partial F_v}{\partial r} + \left(q^2 - \frac{v^2}{r^2}\right)F_v = 0. \tag{2.1.36}$$

The differential equation (2.1.36) is known as the Bessel differential equation and has two linear independent solutions, which are the Bessel function of the first kind $J_v(qr)$ and the Bessel function of the second kind $Y_v(qr)$, sometimes called also Weber or Neumann function and noted as $N_v(qr)$. Also solutions of the modified differential Bessel equation

$$\frac{\partial^2 F_v}{\partial r^2} + \frac{1}{r}\frac{\partial F_v}{\partial r} + \left(-w^2 - \frac{v^2}{r^2}\right)F_v = 0 \tag{2.1.37}$$

are important, which are the modified Bessel function of the first kind $I_v(wr)$ and the modified Bessel function of the second kind $K_v(wr)$, sometimes also known as MacDonald's or Basset function. The number v in all these solutions represents the order of the function.

Electric and magnetic fields of a z-invariant medium with rotational symmetry could be therefore expressed by the Bessel functions or their linear combinations. Important functions are the so called Henkel functions of the first kind $H_v^{(1)}(qr)$ and of the second kind $H_v^{(2)}(qr)$, which are defined as follow:

$$H_v^{(1)}(qr) = J_v(qr) + iY_v(qr) \tag{2.1.38}$$

$$H_v^{(2)}(qr) = J_v(qr) - iY_v(qr) \tag{2.1.39}$$

In each region with a constant refractive index, that means according to (2.1.33) with a constant k and thus, according to (2.1.32), also with a constant q, own solutions of the Maxwell's equations of the form (2.1.34) and (2.1.35) are existing. The order of the used functions v should be thereby in all regions the same because of the boundary conditions on the interfaces between these regions. In the central part of the structure the solutions should be constructed using only the Bessel functions of the first kind, because they are finite at $r = 0$. For the outer regions the modified Bessel functions of the second kind $K_v(wr)$ are suitable, because they disappear as r increases: $K_v(wr) \underset{wr\to\infty}{\longrightarrow} 0$.

So far we have seen which form electric and magnetic fields in a z-invariant rotational symmetric medium should have. No restrictions were met regarding the propagation constant β, so that for each frequency ω infinite number of solutions was possible. By introducing interfaces in the r direction and also by setting the boundary conditions in this direction the propagation constant β becomes discreet. For a given v discreet propagation constants exist:

$$\beta_{v1}, \beta_{v2}, \beta_{v3}, \ldots \tag{2.1.40}$$

For each β_{vm} one solution calling an eigenmode exist. These solutions are denoted by TE_{0m}, TM_{0m}, HE_{vm} or EH_{vm} respectively. For $v = 0$ only TE and TM eigenmodes exist, for $v > 0$ only HE and EH modes. The well known linear polarized LP modes are simplifications of the more common case presented here. They could be used if the differences in refractive indices inside of the investigated structure are small. This is mostly not the case for oxide-confined VCSELs, which is why hybrid modes should be used.

After calculation of eigenmodes in each region with constant refractive index, the electric and magnetic fields can be represented as an infinite sum over the forward and backward propagating eigenmodes:

$$\vec{E}(r,\phi,z) = \sum_k \left(A_k^+ \cdot \vec{E}_k(r,\phi) \cdot e^{-j\beta_k z} + A_k^- \cdot \vec{E}_k(r,\phi) \cdot e^{j\beta_k z}\right), \tag{2.1.41}$$

$$\vec{H}(r,\phi,z) = \sum_k \left(A_k^+ \cdot \vec{H}_k(r,\phi) \cdot e^{-j\beta_k z} + A_k^- \cdot \vec{H}_k(r,\phi) \cdot e^{j\beta_k z}\right). \quad (2.1.42)$$

Here A_k^+ and A_k^- represent expansion coefficients for the forward and backward propagation eigenmode, $\vec{E}_k(r,\phi)$ and $\vec{H}_k(r,\phi)$ are the eigenmode field profiles and β_k is the propagation constant of the eigenmode with index k. In a practical case the number of the used eigenmodes should not be infinite, but a relatively low number of the eigenmodes, depending on the structure and desired precision, is enough to get reasonable results.

Knowing the eigenmodes in every region one can use only the expansion coefficients A_k^+ and A_k^- for the field representation according to Eqs. 2.1.41 and 2.1.42. Thereby in every region own eigenmodes exist and therefore also the expansion coefficients would be different. For interfaces in the z-direction corresponding matrices could be defined, which describe reflection and transmission at each interface, and thus changes of the vector with expansion coefficients while going from one region to another (Fig. 2.9a). For locating the laser modes and calculating of the mode properties, e.g. field distribution, modal volume etc., the VCSEL is divided into two stacks and reflection matrices from both stacks are calculated, as shown in Fig. 2.9b.

A lasing mode should reproduce itself after these two reflections, so that by varying the frequency ω (or the laser light wavelength λ) and the material gain g such field configuration should be found, which satisfies the lasing condition

$$Q = R_{\text{top}} \cdot R_{\text{bot}} = 1. \quad (2.1.43)$$

The eigenmode expansion technique is an exact and three-dimensional tool, which enables to calculate lasing modes of a "cold" cavity, which means without considering electrical or thermal effects. This method is a pure optical but at the same time a very powerful tool, which gives access to the crucial optical parameters of the ground and also higher order lasing modes. In the next sections of this chapter simulation results for different optical phenomena in VCSELs, obtained with the eigenmode expansion technique realized in the CAMFR freeware, will be presented. All simulations were carried out with the number of modes between 200 and 300. The time for one calculation varied depending on complexity of the desired VCSEL structures, precisions, number of calculated

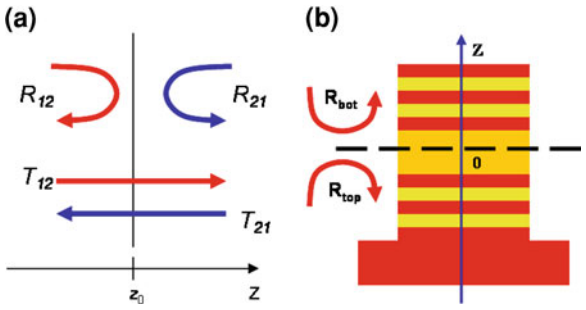

Fig. 2.9 Matrices describing expansion coefficient transformation at interfaces (**a**) and the principle of the laser mode calculation with eigenmode expansion technique (**b**)

pictures etc. between one and several hours, which is a reasonable time effort for a scientist interesting in understanding of important laser phenomena and for efficient VCSEL designing.

2.1.3 Mode Structure of Oxide-Confined VCSELs

Knowing the mode structure and the properties of the ground and higher order lasing modes is of a great importance for an efficient VCSEL designing. Optical properties of laser modes like optical confinement factor and mode volume directly affect CW and modulation characteristics of the fabricated VCSELs. Having a deep understanding of the field distribution for the ground and higher order modes enables to design lasers with proper modal characteristics by using special techniques, for example photonic crystals etched into the top mirror of a VCSEL [24–28], holey VCSELs [29] or VCSELs with surface relief [30–32].

Commonly, VCSELs operate in a single longitudinal mode, but in several transversal modes. In oxide-confined VCSELs, like investigated in this work, optical guiding is realized by the oxide aperture. Oxide-confined VCSELs have established their self because of the reliable and simple fabrication of the oxide aperture and are today commercially available. Mode behavior in oxide-confined VCSELs is strongly dependent on the geometrical parameters of the oxide aperture, e.g. aperture position, thickness, form, diameter and also number of apertures. Using eigenmode expansion technique these effects can be easily calculated for the cold cavity case [33]. Several assumptions should be made in order to be able to use eigenmode expansions. The most important assumption is the homogeneously pumped active region, which is in the reality not the case. The fact that the eigenmode expansion handles only the optical part of a VCSEL restricts the use of the model to achieve quantitative results for physical quantities, which have strongly dependence on electrical and thermal inhomogeneities. Nevertheless for a given temperature and current flow many optical properties of a laser mode, e.g. wavelength, field distribution, mode volume, optical confinement factor etc., remain stable, so that a qualitative picture of the modal behavior of oxide-confined VCSELs could be constructed using fully vectorial three-dimensional optical simulations with the eigenmode expansion technique. This gives a deeper understanding of the physical processes inside of the lasers, which delivers an enormous important contribution to a proper VCSEL design.

First, an overview over the lasing modes existing in an oxide-confined VCSEL will be given. As we have seen in the previous section, in cylindrical structures eigenmodes denoted as TE, TM, HE and EH exist, which have field distributions constructed from the Bessel functions. A laser mode can be expressed in each layer by a sum over the corresponding eigenmodes of this layer. Simulations show, that field profiles of lasing modes have similarities with the eigenmodes. The reason is that in the eigenmode expansion of a lasing mode (2.1.41) and (2.1.42) certain eigenmodes have larger expansion coefficients A_k^+ and A_k^-, and thus play a larger

role. Consequently for the classification of the lasing modes similar notation could be used as for circular cylindrical optical fibers [23]. Therefore we denote the lasing modes by HE_{11}, TE_{01} and so on. The first number in the subscript defines the angular dependence of the electric and magnetic field components according to (2.1.34) and (2.1.35), and thus also the order of the Bessel functions used in the eigenmode expansion of this lasing mode. The second number in the subscript denotes the sequence number of the mode. For example for the angular number 1 following lasing modes will exist: HE_{11}, EH_{11}, HE_{12}, EH_{12}, HE_{13}, EH_{13} and so on. We note that for the angular number 0 only TE and TM modes exist, while for angular numbers larger than 0 only HE and EH modes exist. To investigate the mode structure of oxide-confined VCSELs calculations based on a simple VCSEL with one 18.8 nm (1/20 part of the lasing wavelength in GaAs) thick oxide aperture placed in the electric field intensity anti-node, a $3/2\lambda$ thick AlGaAs-based cavity and 25/30 $Al_{0.90}GaAs/GaAs$ top/bottom DBR pairs without any gradings were carried out. The diameter of the oxide aperture was for these simulations 8 μm, enabling lasing of several higher order modes. The diameter of the homogonously pumped active region was also 8 μm. Since the calculations were made for the cold cavity case, the absolute numbers for the threshold material gain should be handled with care. The ground mode and several higher order modes, altogether 21 modes, for the angular numbers from 0 up to 7 were calculated. Obtained wavelength and threshold material gain for each calculated mode are shown in Fig. 2.10.

From the picture is seen, that the lasing mode with the longest wavelength and with the smallest threshold material gain is the HE_{11} mode, which is the ground mode of the laser. Then three modes (TE_{01}, TM_{01} and HE_{21}) with practically identical wavelengths (1093.63, 1093.65 and 1093.64 nm, respectively) follow. In scalar models these three modes are not resolved and handled as one LP_{11} mode. As we will see later these three modes have very similar radial intensity distribution, but different field profiles. Then other lasing modes

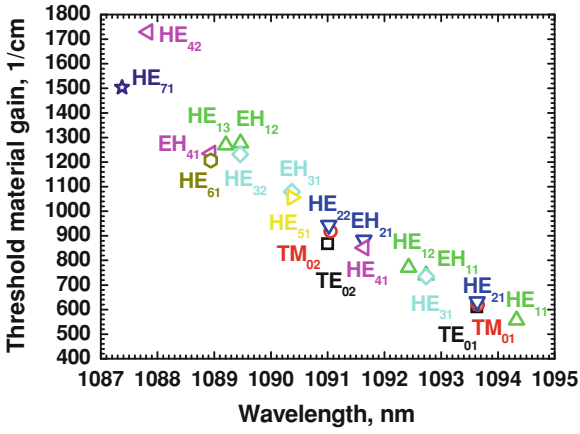

Fig. 2.10 Calculated wavelength and threshold material gain for a number of lasing modes for an oxide-confined VCSEL emitting around 1,100 nm

with shorter wavelengths follow, from which again some have similar wavelengths and intensity distributions and build groups of modes. As one can see from Fig. 2.10 each two modes of the type EH_{mn} and $HE_{m+2,n}$ belong to a single group, for example $EH_{11}$and HE_{31}or EH_{12} and HE_{32}. Also modes of the type TE_{0n}, TM_{0n} and HE_{2n} belong together. HE-modes with the angular number 1 stay alone, like HE_{11}, HE_{12} or HE_{13}. Because only limited number of the higher order modes was calculated, not every group is shown complete. The threshold material gain increases for higher order modes because the field distribution moves to the outer regions and the overlap with the pumped active region decreases.

In Fig. 2.11 field profiles in a transverse plane inside of the cavity for the ground and higher order modes from the Fig. 2.10 are shown. Different symmetries can be observed by taking a look at the field profiles of different modes and comparing modes with the same angular number m as well as modes with different angular number but with the same sequence number n. The ground mode HE_{11} has a Gaussian-like profile and is linear polarized.

It is also of a great importance to know the radial intensity distribution for the ground and the higher order modes, which is shown in Figs. 2.12 and 2.13.

For higher order modes the intensity distribution moves from the center to outer regions, although this trend is not strongly regular. Lasing modes, which belong to the same group, have similar radial intensity distribution, for example TE_{01}, TM_{01} and HE_{21}. To get the better overview over the three-dimensional field distributions, electric field amplitudes for the ground mode HE_{11} and the first order mode TE_{01} for the same VCSEL are shown in Fig. 2.14.

The cylindrical symmetry of oxide-confined VCSELs in the reality could be disturbed during the fabrication, for example during the formation of the oxide aperture by the wet oxidation, depending on the oxidation parameters. Commonly, for large enough aperture diameters this effect becomes small, so that the mode structure remains similar to the case investigated here. Of course it could be desirable in some cases not to have the cylindrical symmetry, for example for polarization stabilization. Breaking the symmetry can be easily achieved by fabricating VCSELs with square mesas or by using other methods. In any case having a deeper understanding of the mode structure and the corresponding field profiles of the ground and the higher order modes enables to design optical properties of the VCSELs more efficiently.

2.1.4 Calculation of the Lasing Mode Parameters

By a known field distribution of a lasing mode important optical parameters can be calculated, which then can be used for device characterization and optimization. Decisive optical mode parameters are the effective mode volume V_{eff} and the three-dimensional optical confinement factor Γ. Both quantities play a major role for CW and high frequency operation of a semiconductor laser. The effective

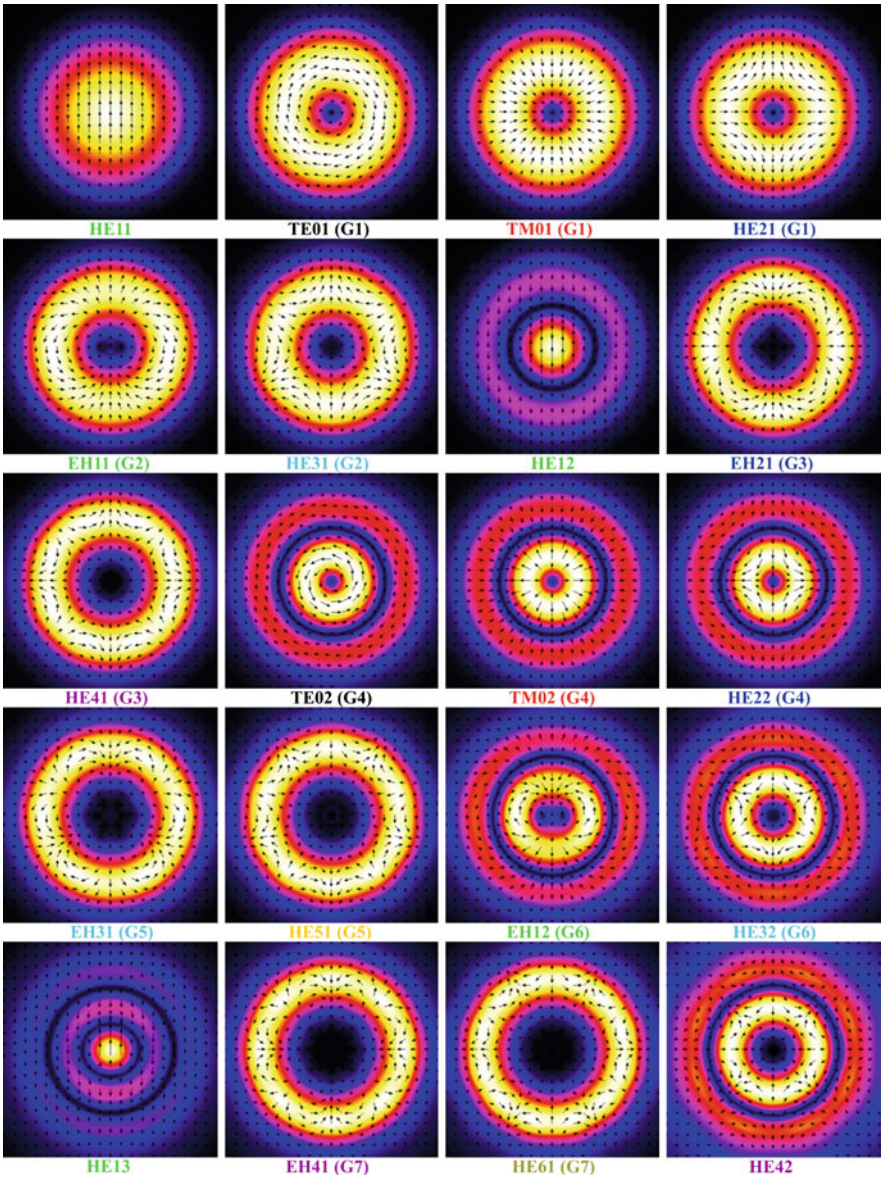

Fig. 2.11 Electrical field distribution in a transverse plane inside of the VCSEL cavity for 8 μm aperture diameter; the dimensions of each figure are 10 × 10 μm, the symmetry axis (z-axis) goes through the central point of each figure out of the figure plane, in brackets the group number is indicated

mode volume for each lasing mode can be calculated from the field distribution of this mode and the refractive index profile of the simulated structure using the formula [34]

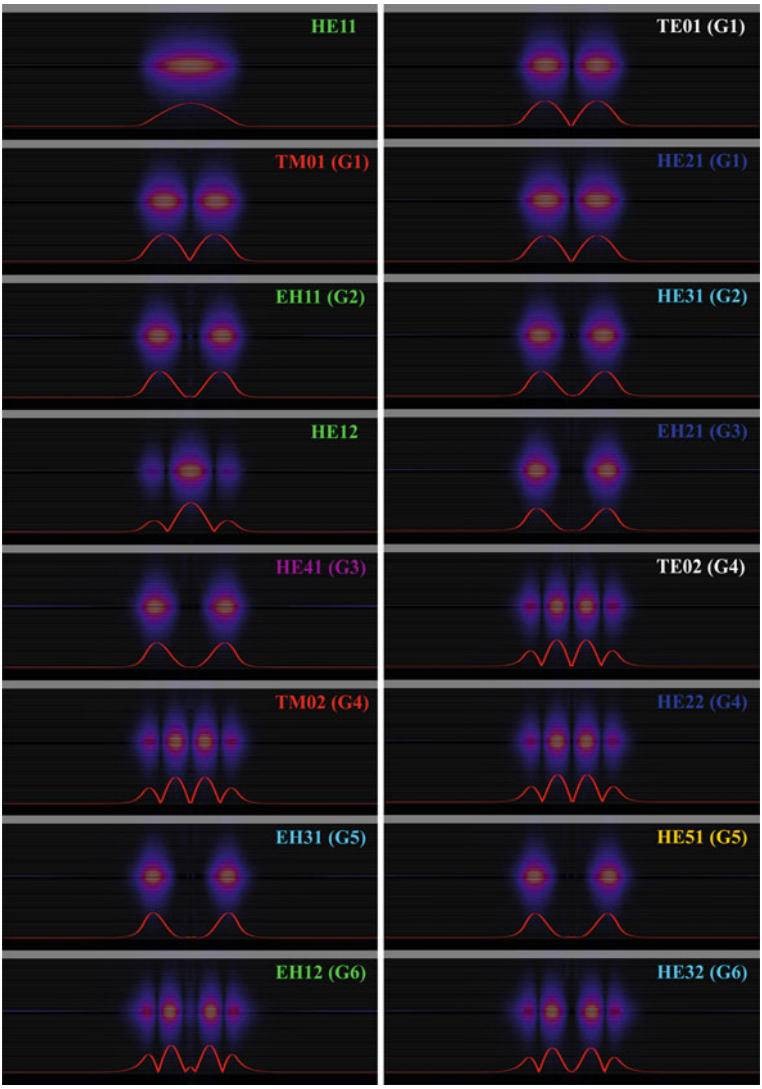

Fig. 2.12 Radial intensity profiles in the r–z-plane and radial electric field amplitudes (*red lines*) of the ground and the higher order modes for the VCSEL with 8 μm oxide aperture diameter; the width of each figure is 32 μm, the symmetry axis (z-axis) goes vertically across the center of each figure

$$V_{\text{eff}} = \frac{\iiint_{\text{cavity}} \varepsilon(\vec{r}) \left|\vec{E}(\vec{r})\right|^2 d^3\vec{r}}{\max\left(\varepsilon(\vec{r}) \left|\vec{E}(\vec{r})\right|^2\right)}. \tag{2.1.44}$$

As can be obtained from Eq. 2.1.44 the effective mode volume is the volume of the cavity weighted by the electrical field power density, which is directly

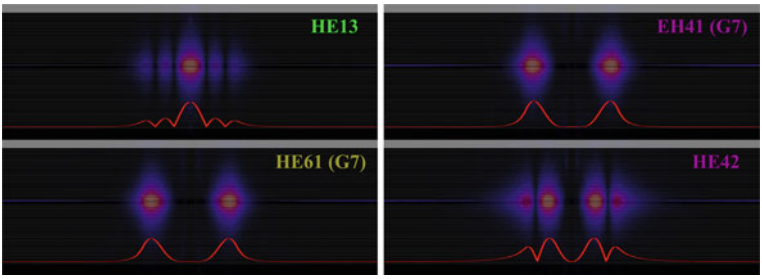

Fig. 2.13 Radial intensity profiles in the r–z-plane and radial and electric field amplitudes (*red lines*) of the higher order modes for the VCSEL with 8 μm oxide aperture diameter; the width of each figure is 32 μm, the symmetry axis (z-axis) goes vertically across the center of each figure

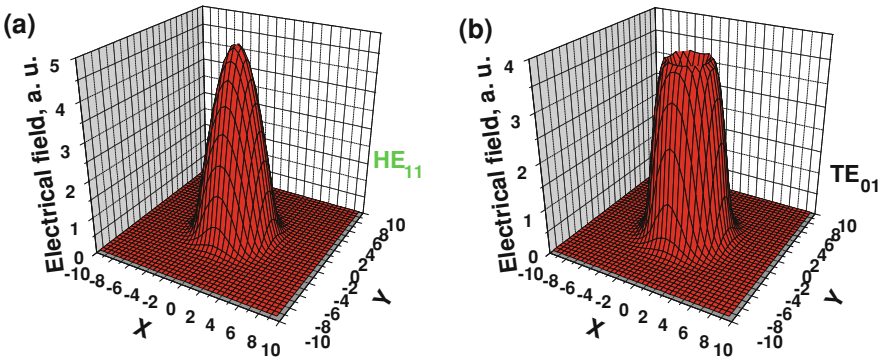

Fig. 2.14 Electric field amplitude for the ground mode (**a**) and the first order mode (**b**) for the oxide-confined VCSEL with 8 μm oxide aperture diameter

proportional to the number of photons used in the rate equations described in the following sections. As we will see later, the effective volume enters equations characterizing the high speed properties of directly modulated lasers. The three-dimensional optical confinement factor is the ratio of the volume of the pumped active region, again weighted by the electrical field power density, to the effective mode volume, as given by the following equation

$$\Gamma = \frac{\iiint_{\text{active}} \varepsilon(\vec{r}) \left|\vec{E}(\vec{r})\right|^2 d^3\vec{r}}{\iiint_{\text{cavity}} \varepsilon(\vec{r}) \left|\vec{E}(\vec{r})\right|^2 d^3\vec{r}}. \tag{2.1.45}$$

Additional to the three-dimensional optical confinement factor Γ also one-dimensional confinement factor Γ_Z can be calculated using one-dimensional methods, for example the transfer matrix method considered above:

$$\Gamma_Z = \frac{\int_{\text{active}} \varepsilon(z)\left|\vec{E}(z)\right|^2 dz}{\int_{\text{cavity}} \varepsilon(z)\left|\vec{E}(z)\right|^2 dz}. \tag{2.1.46}$$

The one-dimensional confinement factor Γ_Z represents commonly the best case value which the three-dimensional confinement factor Γ can achieve in a VCSEL, because of the additional edge effects in the three-dimensional case.

Very helpful for the understanding of the optical properties of VCSELs is a qualitative dependence of these parameters on the oxide aperture diameter. For this purpose, simulations on two simple 850 nm VCSEL structures with 24/35 top/bottom $Al_{0.15}Ga_{0.85}As/Al_{0.90}Ga_{0.10}As$ DBR pairs without any gradings were carried out. To investigate the dependence of the effective mode volume and the optical confinement factor on the cavity length one of the simulated structure was chosen to have a 1λ AlGaAs based cavity, the second structure had a 2λ cavity. For comparison of the three-dimensional and one-dimensional confinement factors and also of the wavelengths one-dimensional simulations with the transfer matrix method were carried out as well.

In Fig. 2.15 wavelength and optical confinement factors are given for the ground mode HE_{11} and the first order mode TE_{01}. For comparison one-dimensional values are also shown by blue lines and corresponding numbers.

From the figure one can see that the three-dimensional values both for the wavelength and for the optical confinement factor are smaller than the corresponding one-dimensional numbers. With increasing aperture diameters the three-dimensional values come closer to the one-dimensional case, because the fields become more similar to the plane wave approximation. Another issue is that for a homogeneously pumped active region with the diameter of the pumped zone 2 μm larger than aperture, like in the case of the presented simulations, the optical confinement factor of the first order mode is smaller than for the ground mode. This can be explained by the field distribution of both modes. Optical energy is

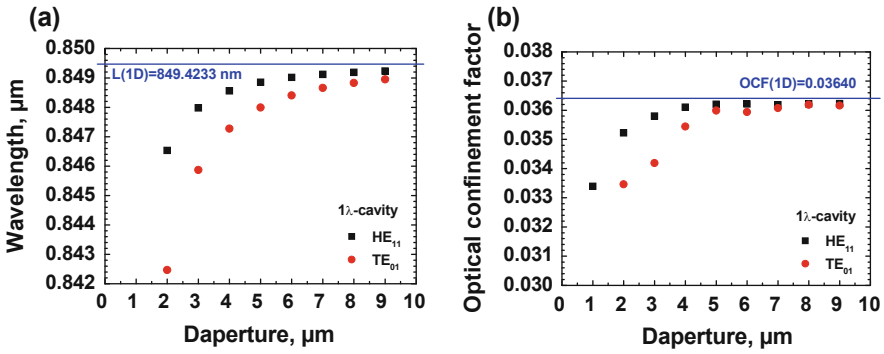

Fig. 2.15 Wavelength (**a**) and optical confinement factor (**b**) for the ground mode (*black squares*) and the first order mode (*red circles*) as a function of the aperture diameter for the 1λ cavity VCSEL; *blue lines* and *numbers* represent one-dimensional values

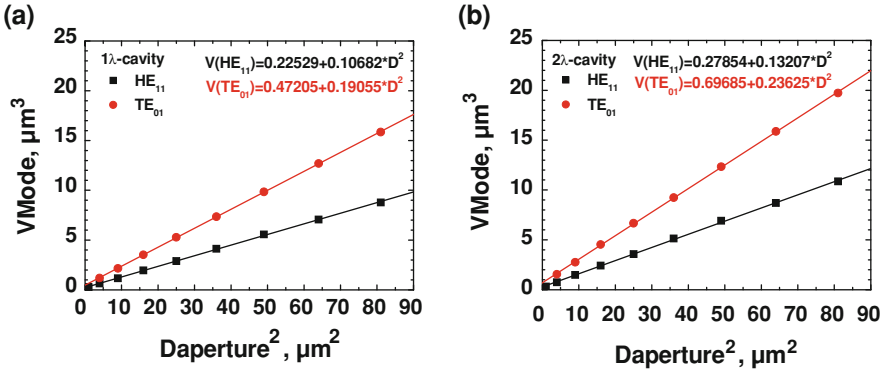

Fig. 2.16 Effective mode volume for the 1λ cavity VCSEL (**a**) and for the 2λ cavity VCSEL (**b**) for the ground and the first order modes as a function of the squared aperture diameter, together with linear fits and corresponding formulas

concentrated for the HE_{11} mode closer to the center as for the TE_{01} mode (see Fig. 2.11 and Fig. 2.12). Very interesting is also the dependence of the effective mode volume on the aperture diameter for both modes, which is shown in Fig. 2.16.

One can see that both modes have linear dependence of the effective mode volume on the squared aperture diameter, i.e. on the aperture area. An offset for both effective mode volumes for both devices is present, as can be obtained from the formulas shown on the figures. It can be explained by the fact that a part of the optical energy is located outside of the aperture region, so that at zero aperture diameters this part would contribute to the mode volume. The smallest aperture diameter investigated was 1 μm and it fits also to the linear dependence. The offset is logically larger for the TE_{01} mode, because this mode has more energy located in the outside regions. Mode volumes for the TE_{01} are also larger compared to the HE_{11} mode, because the first order mode is weaker confined. The linear dependence of the mode volume on the aperture diameter can be experimentally proved by measurement of the parameters which depend on the effective mode volume, for example the D-factor. These measurements will be described in the later chapters.

The slope of both curves is larger for the longer VCSEL, because of the larger cavity length. The slope of the effective mode volume for the HE_{11} mode is 0.10682 for the 1λ cavity and 0.13207 for the 2λ cavity. The effective cavity length calculated with the transfer matrix method is 0.4783 μm for the shorter device and 0.5917 μm for the longer one. The ratio of the slopes of the linear fits for the ground mode 0.13207/0.10682 is 1.236 and practically perfectly agrees to the ratio of the effective cavity lengths of 0.5917/0.4783, which is 1.237. This fact shows that the differences in the slope of the effective mode volume curves of the ground mode are mainly caused by the differences in the effective cavity lengths of the VCSELs.

Thus one can see that one-dimensional and three-dimensional simulations are powerful tools to deliver the knowledge about important parameters of the lasing modes. This helps by the characterization, optimization and understanding of the optical phenomena inside of VCSELs, since optical processes in the devices are complicated and versatile. Nevertheless optics is only one of the many sides of semiconductor lasers, and in the next sections electrical and thermal phenomena will be considered.

2.2 Electrical Properties

Semiconductor lasers are devices which convert electrical energy in the optical energy, thus optoelectronic devices. This means that additional to the optical phenomena considered in the previous sections, also electrical phenomena play a tremendous role in the semiconductor lasers. As in the case of the optical properties, electrical properties are also determined by the design of both epitaxial structure and of the fabricated device. While in the case of the optical properties in oxide-confined VCSELs the main influence during the fabrication comes from the formation of the oxide aperture, more effects contribute to the electrical properties of the fabricated devices, especially on the high frequency side. Such parameters, which are determined by the device design, like dimensions and position of the contacts, dimensions of the contact pads, properties of the applied dielectric layers, play a decisive role for the electrical properties of the lasers. That is why it makes sense to distinguish between the electrical properties, which should be considered during the designing of the epitaxial growth structure, and external electrical properties of the fabricated devices, which act mostly as a limitation of the internal electrical properties. In the next three sections we will describe designing of the internal electrical properties of the epitaxial structure, while in the following two sections external effects will be considered. During the designing process of any semiconductor lasers with active elements of dimensions, where quantum effects play a significant role, for calculation of the corresponding properties quantum mechanics should be applied. This is the fact for QW-regions, and thus we will consider quantum mechanic effects also in the following sections. In the sections handling the electrical properties we will not use the phasor notation, so that all quantities are real physically values.

2.2.1 Carrier Dynamic in Semiconductor Lasers

We start again with the Maxwell's equations (2.1.1–2.1.4) [1, 35]. For quasi-electrostatic fields, that means for fields with slow time variation, one can neglect the time derivatives in Eqs. 2.1.1 and 2.1.2 and for the case of absent or negligible magnetic field ($\vec{H} \cong 0$, $\vec{B} \cong 0$) for electric field two equations will stay:

$$\vec{\nabla} \times \vec{E} = 0, \tag{2.2.1}$$

$$\vec{\nabla} \cdot \vec{D} = \rho. \tag{2.2.2}$$

The solution for the electric field can be expressed in this case by a gradient of a scalar function φ, which is called electrostatic potential:

$$\vec{E} = -\vec{\nabla}\varphi, \tag{2.2.3}$$

Inserting (2.2.3) into (2.2.2) and using (2.1.6) for an isotropic medium we get the Poisson's equation for the electrostatic potential:

$$\vec{\nabla} \cdot \left(\varepsilon \vec{\nabla}\varphi\right) = -\rho. \tag{2.2.4}$$

By higher frequencies one may include the displacement current density $\vec{J}_{\text{disp}}$ to the conduction current density, so that for the total current density $\vec{J}_{\text{tot}}$ the following equation holds:

$$\vec{J}_{\text{tot}} = \vec{J}_{\text{con}} + \vec{J}_{\text{disp}} = \vec{J}_{\text{con}} + \frac{\partial}{\partial t}\left(\varepsilon \vec{E}\right). \tag{2.2.5}$$

The charge density ρ can be expressed in a semiconductor by a sum over the electron concentration n, the hole concentration p and concentrations of the positive charged ionized donors N_D^+ and the negative charged ionized acceptors N_A^- with appropriate electrical charge sign:

$$\rho = q\left(p - n + N_D^+ - N_A^-\right), \tag{2.2.6}$$

where q stay for the magnitude of the unit charge and is $q = 1.6 \times 10^{19}$ C. One can divide the conduction current density into two parts representing electron and hole conduction current densities $\vec{J}_n$ and $\vec{J}_p$ respectively:

$$\vec{J}_{\text{con}} = \vec{J}_p + \vec{J}_n. \tag{2.2.7}$$

By a time-independent total doping concentration $C_0 = N_D^+ - N_A^-$ one can divide the continuity equation (2.1.5) for the conduction current into two parts for electrons and holes:

$$\vec{\nabla} \cdot \vec{J}_n - q\frac{\partial}{\partial t}n = qR, \tag{2.2.8}$$

$$\vec{\nabla} \cdot \vec{J}_p + q\frac{\partial}{\partial t}p = -qR, \tag{2.2.9}$$

with the net recombination rate of electron–hole pairs per unit volume R given by

$$R = R_n - G_n = R_p - G_p \tag{2.2.10}$$

with the generation (G_n and G_p) and recombination (R_n and R_p) rates for electron and holes separately. Thus for each kind of the charge carriers continuity equation can be written:

$$\frac{\partial}{\partial t}n = G_n - R_n + \frac{1}{q}\vec{\nabla}\cdot\vec{J}_n, \tag{2.2.11}$$

$$\frac{\partial}{\partial t}p = G_p - R_p - \frac{1}{q}\vec{\nabla}\cdot\vec{J}_p. \tag{2.2.12}$$

For the flow of charge carriers drift–diffusion model can be used, which consider two major mechanisms of the carrier transport. The first is the drift current which is generated by an electrical field and is directly proportional to the conductivity of electrons $\sigma_n = q\mu_n n$ and holes $\sigma_p = q\mu_p n$, where μ_n and μ_p are the electron and hole mobility, respectively. By a present concentration gradient of electron or holes diffusion current will appear, which is directly proportional to the diffusion coefficient of the electrons D_n and holes D_p. Mobility and diffusion coefficients are related by the Einstein relation

$$\frac{D_n}{\mu_n} = \frac{D_p}{\mu_p} = \frac{kT}{q}, \tag{2.2.13}$$

where T is the temperature of the material and k is the Boltzmann constant $k = 1.3807 \times 10^{-23}$ J/K. The total current density of electron and holes can be then written as

$$\vec{J}_n = q\mu_n n\vec{E} + qD_n\nabla n, \tag{2.2.14}$$

$$\vec{J}_p = q\mu_p p\vec{E} - qD_p\nabla p, \tag{2.2.15}$$

Inserting (2.2.14) and (2.2.15) into (2.2.11) and (2.2.12) and using electrostatic potential (2.2.3) instead of the electric field allows us to reduce the number of unknowns to only three scalar functions $n(\vec{r})$, $p(\vec{r})$ and $\varphi(\vec{r})$:

$$\frac{\partial}{\partial t}n = G_n - R_n + \frac{1}{q}\vec{\nabla}\cdot\left(q\mu_n n\vec{\nabla}\varphi + qD_n\vec{\nabla}n\right), \tag{2.2.16}$$

$$\frac{\partial}{\partial t}p = G_p - R_p - \frac{1}{q}\vec{\nabla}\cdot\left(q\mu_p p\vec{\nabla}\varphi - qD_p\vec{\nabla}p\right), \tag{2.2.17}$$

$$\vec{\nabla}\cdot\left(\varepsilon\vec{\nabla}\varphi\right) = -q\left(p - n + N_D^+ - N_A^-\right). \tag{2.2.18}$$

By specified boundary conditions Eqs. 2.2.16–2.2.18 can be solved and will deliver the three unknowns. Inside of the laser the carrier concentrations can vary by many orders of magnitude. That is why they are often replaced by the quasi-Fermi levels F_n and F_p for electrons and holes, respectively. They can be

calculated in a common case using the Fermi–Dirac statistics for electrons f_n and holes f_p, the corresponding densities of states ρ_e and ρ_h and the following equations:

$$n = \int_{-\infty}^{\infty} f_n(E)\rho_e(E)dE, \tag{2.2.19}$$

$$p = \int_{-\infty}^{\infty} f_p(E)\rho_h(E)dE, \tag{2.2.20}$$

with

$$f_n(E) = \frac{1}{1 + e^{(E-F_n)/kT}}, \tag{2.2.21}$$

$$f_p(E) = \frac{1}{1 + e^{(F_p-E)/kT}}. \tag{2.2.22}$$

One can express the quasi-Fermi levels for electrons F_n and holes F_p by corresponding potentials according to the following equations:

$$F_n(\vec{r}) = -q\varphi_n(\vec{r}) + E_{ref}, \tag{2.2.23}$$

$$F_p(\vec{r}) = -q\varphi_p(\vec{r}) + E_{ref}, \tag{2.2.24}$$

with a reference constant energy E_{ref} and handle the three unknowns $\varphi(\vec{r})$, $\varphi_n(\vec{r})$ and $\varphi_p(\vec{r})$, which have the same units (volts).

Using the drift–diffusion model one can efficiently design epitaxial structure of a VCSEL and optimize DBR layers and the cavity region. For designing of the active region quantum mechanics should be applied. In the next two sections one-dimensional calculations for the epitaxial VCSEL design optimization, carried out with the free software Nextnano++ [36], are presented. The used software includes a solver for the Poisson's and current equations and has quantum mechanical solver for the active region as well. It is simple to use and is very fast, thus perfectly suited for such kinds of applications.

2.2.2 Electrical Design of the DBR Mirrors

The largest part of the epitaxial VCSEL structure consists of DBR mirrors, both top and bottom. DBR mirrors contain also the most number of interfaces of a VCSEL structure. That is why a proper and careful electrical design of both mirrors is of a great importance. Since the thicknesses of the DBR-layers are mainly defined by the wavelength of the laser light, the main objective of electrical

simulations is to improve the conductivity of the mirrors, mainly by reducing potential barriers at the interfaces, which arise from the different material compositions and thus different band gaps of the corresponding materials used in the DBR mirrors. For the VCSELs presented in this work Al-compositions of 12, 15 and 90% additional to pure GaAs were used. We will describe optimization of the DBR mirror structure on the example of the 980 nm QW-VCSELs investigated in this work.

Immense work was done in the past for optimization of the interfaces inside a DBR mirror [37]. Different schemes were investigated, for example linear gradings (LG) at the interfaces or bi-parabolic gradings. While the second scheme is more difficult to realize, linear gradings can be grown without big effort by standard metal–organic chemical vapor deposition (MOCVD) technique. In the case of the molecular beam epitaxy (MBE) digital gradings should be applied, but it can be realized as well. In this work, for all structures linear gradings of 10 or 20 nm thickness for both top and bottom DBR mirrors were applied.

In Fig. 2.17 Al-composition for an $Al_{0.12}Ga_{0.88}As/Al_{0.90}Ga_{0.10}As$ DBR mirror without and with 20 nm thick linear gradings is presented. The total thickness of each DBR pair is kept constant. The corresponding band structures are shown in Fig. 2.18 for the case without gradings (a) and with the 20 nm thick gradings (b) for intrinsic material. In the following pictures only two periods of the DBR mirrors are shown for more clarity.

In Fig. 2.18 energies of different minima and maxima in conduction and valence bands are shown. Electrons can occupy the minima around the Γ, X and L points in the conduction band. Holes occupy the maxima in the heavy-hole (HH), light-hole (LH) or split-off (SO) valence bands. For Al-compositions from 0 up to ∼40–45% AlGaAs has a direct band gap, for higher compositions AlGaAs becomes an indirect semiconductor with the X minima having the lowest energy in the conduction band.

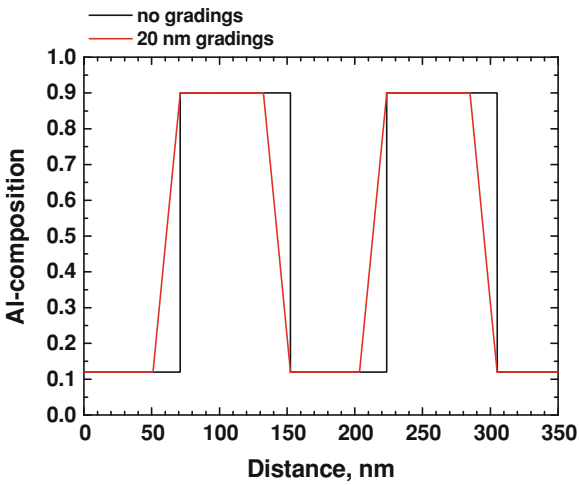

Fig. 2.17 Al-composition of an $Al_{0.12}Ga_{0.88}As/Al_{0.90}Ga_{0.10}As$ DBR mirror without and with 20 nm thick linear gradings

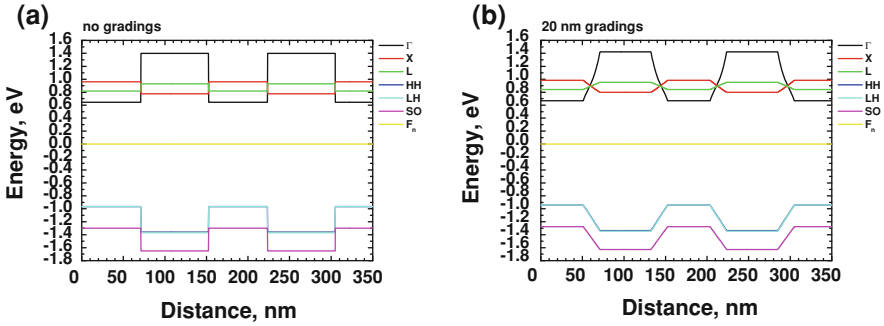

Fig. 2.18 Band structure of the DBR mirror without (**a**) and with 20 nm thick linear gradings (**b**) for intrinsic materials

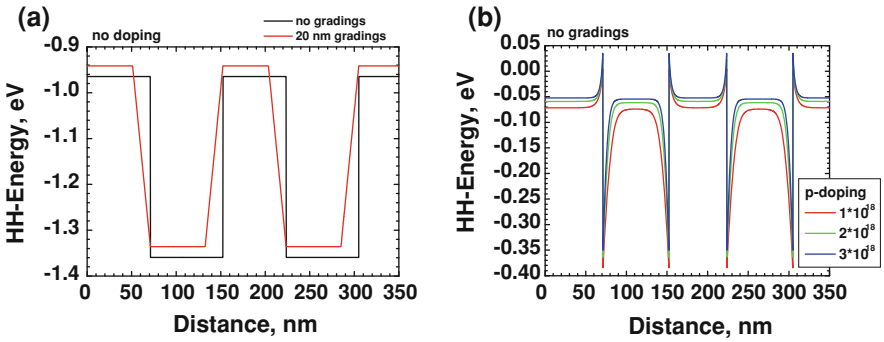

Fig. 2.19 Energy of the heavy-hole band minimum for the DBR mirror with and without linear gradings for intrinsic semiconductor (**a**) and for the DBR mirror without gradings for different levels of the p-doping (**b**)

From the Fig. 2.18 one can see considerable potential barriers between materials with different Al-composition for both electrons in the conduction band and holes in the valence band. In Fig. 2.19a, the zoomed view of the heavy-hole band minimum for intrinsic materials for the cases without and with linear gradings is shown. The height of the potential barrier for holes reaches $\sim$0.4 eV. If one considers the total number of the interfaces in a typical DBR mirror, which varies in the range of 40–70 for 20 and 35 DBR pairs respectively, one can immediately see the importance of reducing the barriers. The commonly used solution is to dope the corresponding mirror whether with donors for the n-type DBR or acceptors for the p-type mirror. In the Fig. 2.19b energy of the heavy-hole band minimum is shown for the case of different p-type doping levels of 1×10^{18}, 2×10^{18}, and 3×10^{18} cm^{-3}, which are typical doping levels for DBR mirrors.

With the present p-doping the situation with the interfaces improves drastically. The difference in the heavy-hole band minimum energies for materials with different composition practically vanishes, and only very thin barriers stay.

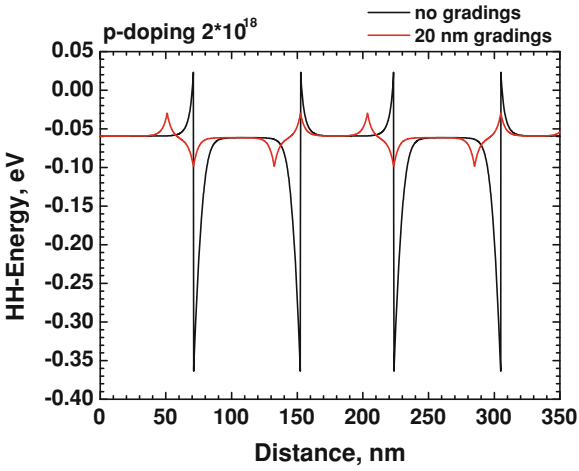

Fig. 2.20 Energy of the heavy-hole band minimum for the p-doping level of 2×10^{18} cm^{-3} for the DBR mirror without and with 20 nm thick linear gradings

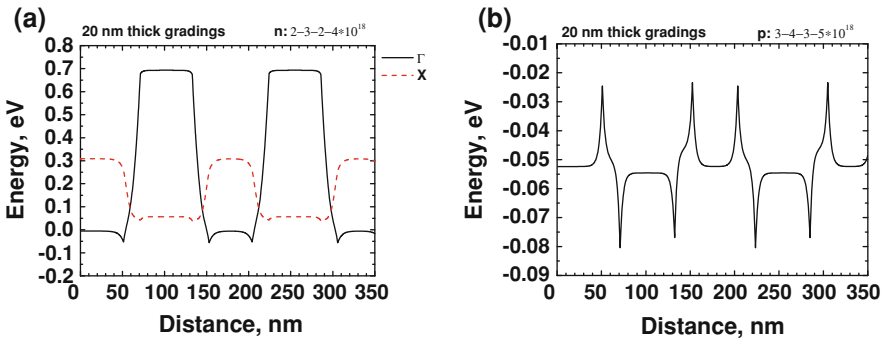

Fig. 2.21 Energy of the Γ and X points of the conduction band for the n-doped DBR mirror (**a**) and energy of the heavy-hole band minimum for the p-doped DBR mirror (**b**)

The thickness of the residual barriers depends on the doping level. Hereby the difference between the doping levels of 2×10^{18} and 3×10^{18} cm^{-3} become smaller as compared to the difference between 1×10^{18} and 2×10^{18} cm^{-3}. Remaining barriers are reduces further for the DBR mirrors with the linear gradings, as shown in Fig. 2.20 for the p-doped mirror and Fig. 2.21 for the n-doped mirror.

The barrier height is reduced from ~0.38 eV down to ~0.07 eV for one p-doped interface. After consideration of the simulation results, doping concentrations of 2×10^{18} cm^{-3} and higher for both n-type and p-type DBR mirrors were chosen for the 980 nm QW-VCSELs. These doping levels are sufficient to reduce the barriers and from the other side do not increase absorption losses in a drastically way. In the first few DBR mirror pairs close to the cavity the doping was leaved at 2×10^{18} cm^{-3}, while moving further away from the cavity into the

region, where the photon density decreases, enables to use higher doping levels. Hereby for interfaces, where electrical field has a node, higher doping levels can be used as for interfaces, in which electrical field has an anti-node. For the investigated structure n-doping levels following the scheme 2–3 to 2–4 $\times$ 10^{18} cm^{-3}, for the corresponding composition scheme $Al_{0.12}Ga_{0.88}As$-LG-$Al_{0.90}Ga_{0.10}As$-LG, was applied. For the p-type DBR the doping levels were 3–4 to 3–5 $\times$ 10^{18} cm^{-3}.

Simulation results presented in this section show, that by introducing linear gradings into the DBR mirrors potential barriers can be effectively suppressed. Linear gradings are an effective and relatively easy to realize solution for low resistance multilayered mirrors for both n- and p-type DBRs.

2.2.3 Design of the Active Region

The part of a semiconductor laser, in which electrical power is converted to the optical power, is the active region. Physical properties of the active region determine in a decisive way the properties of the laser, both for CW and high frequency modulation. That is why special attention must be paid while designing the active region. We will describe this again using the 980 nm QW-VCSELs as example.

Quantum mechanics should be applied in order to be able to describe physical properties of QWs correctly. The basic nonrelativistic quantum mechanical equation is the well-known Schrödinger equation [1, 2, 35], which for a static case and one particle has the form

$$H\Psi = E\Psi, \tag{2.2.25}$$

with

$$H = -\frac{\hbar^2}{2m}\nabla^2 + V(\vec{r}). \tag{2.2.26}$$

Here H is the quantum mechanical operator called Hamiltonian, $\hbar$ is the Planck constant h divided by 2π, and m is the mass of the desired particle. The solution of the Schrödinger equation for some energy value E is the corresponding Ψ-function, also called the wave function, describing all physical properties of the quantum mechanical state of the particle. $V(\vec{r})$ is the potential energy function, which defines the particle motion.

In the case of semiconductor lasers considered particles are electrons and holes. For a simpler description we can use in the first approximation energy of the corresponding minima and maxima in the conduction and valence bands as potential energy and so-called effective masses of the carriers instead of the masses of free particles. This enables to use the simple Eqs. 2.2.25 and 2.2.26 and at the same time to include effects corresponding to the band structure. Also more

advanced models like 8-band k*p theory [1] can be applied for more exact calculations. Nextnano++ is able to calculate energy states using both classical method using effective carrier masses and the 8-band k*p method.

The most important property which should be calculated is the emission wavelength of the laser. In the case of a VCSEL the wavelength of the emitted light is defined by the cavity dip position, thus by the optical properties of the cavity, described in the previous sections. Nevertheless the active medium used in the VCSEL should be able to emit photons at this wavelength; otherwise no lasing would take place. Because of the temperature effects, the peak of the stimulated emission in the active region should be designed to be at a shorter wavelength compared to the cavity dip wavelength. The reason is the stronger temperature shift of the band gap of AlGaAs compared to the shift of the wavelength of the cavity dip. Because internal temperatures in VCSELs can easily reach 80–100°C, detuning between the cavity dip wavelength and the peak emission wavelength of the active region is commonly in the range of 5–20 nm. For a stable high temperature operation rather larger values should be considered. From 980 nm QW-VCSELs described in this work nominal value of the cavity-gain detuning was 15 nm, thus the peak emission wavelength of the active region was calculated to be at 965 nm. At this wavelength strained InGaAs QWs can be used. After some calculations the In-composition of 21% by the QW-thickness of 4.2 nm was determined. For strain compensation 6 nm thick GaAsP layers acting at the same time as barriers between QWs with P-composition of 12% were applied. Figure 2.22 shows the corresponding bands for the active region considered here. Because of the strain the HH and LH valence bands are splitted.

By solving the Schrödinger equation with the effective masses of the corresponding band minima and maxima eigenvalues of the energy states and corresponding Ψ-functions were calculated. Hereby only the first five solutions for each electrons and holes, together ten solutions, were investigated. They correspond to the ground levels in the conduction and valence bands. Figure 2.23 shows the calculated energy levels for electrons (a) and holes (b).

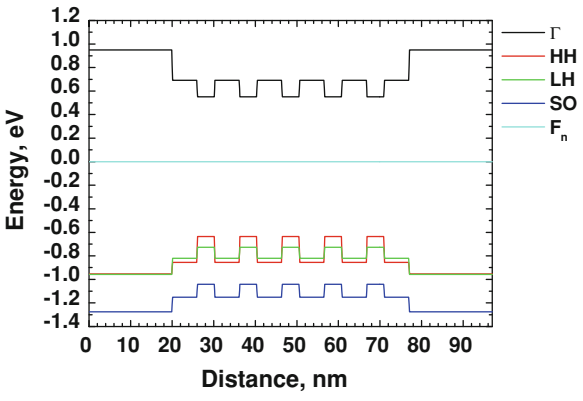

Fig. 2.22 Energy diagram of the active region consisting of five 4.2 nm thick $In_{0.21}Ga_{0.79}As$ QWs with 6 nm thick $GaAs_{0.88}P_{0.12}$ barriers acting simultaneously as strain compensation layers; the outer region consist on each side of 20 nm $Al_{0.35}Ga_{0.65}As$

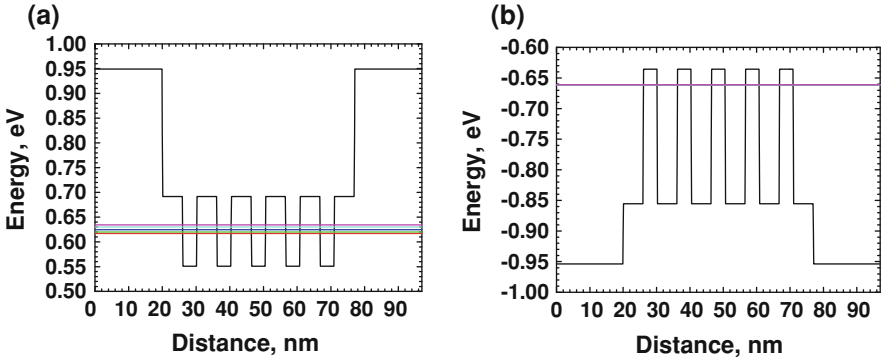

Fig. 2.23 Energy states in the conduction (**a**) and the heavy-hole (**b**) band for electrons and holes respectively

The QWs are partially coupled, as can be seen from the energy levels, which has slightly different energy values. Energy levels of the hole states have practically identical values. Figure 2.24 shows the first four energy levels with the corresponding wave functions for the electrons in the conduction band. Corresponding hole states and wave functions are shown in Fig. 2.25.

As one can see from the Figs. 2.24 and 2.25, the form of the corresponding wave functions of electrons and holes is similar and their overlap is large, resulting in an efficient stimulated photon emission.

Finally the difference between the lowest electron energy level and the highest hole energy level should be calculated in order to determine the emission wavelength. In Fig. 2.26 the energy difference between the ground electron and hole levels as a function of the temperature, calculated with the effective mass theory (black) and with the more precisely 8-band k*p theory (red), is shown. For a better orientation the goal wavelength of the active region peak emission at room temperature of 965 nm (green line), the wavelength of the room temperature VCSEL emission determined by the cavity dip wavelength at 980 nm (blue dotted line) and the temperature dependent cavity dip wavelength (blue solid line) are also shown. Considered was a temperature range between 300 and 400 K, which corresponds approximately to temperatures from the room temperature up to ~120°C. Since the cavity dip also moves with the temperature, the best resonance between the active region peak gain and the cavity dip will appear not at the internal VCSEL temperature of ~345 K, corresponding to ~70°C, but at a higher temperature. Since internal temperatures of ~70°C are reached at the ambience temperatures of ~20–30°C, for a better temperature stability and an efficient operation at ambience temperatures of 80–100°C, which result in internal laser temperatures of 130–150°C, or ~400–420 K, perfect detuning should be designed to lay somewhere between 340 and 400 K. Assuming an approximately fourfold weaker dependence of the cavity dip wavelength on temperature, as compared

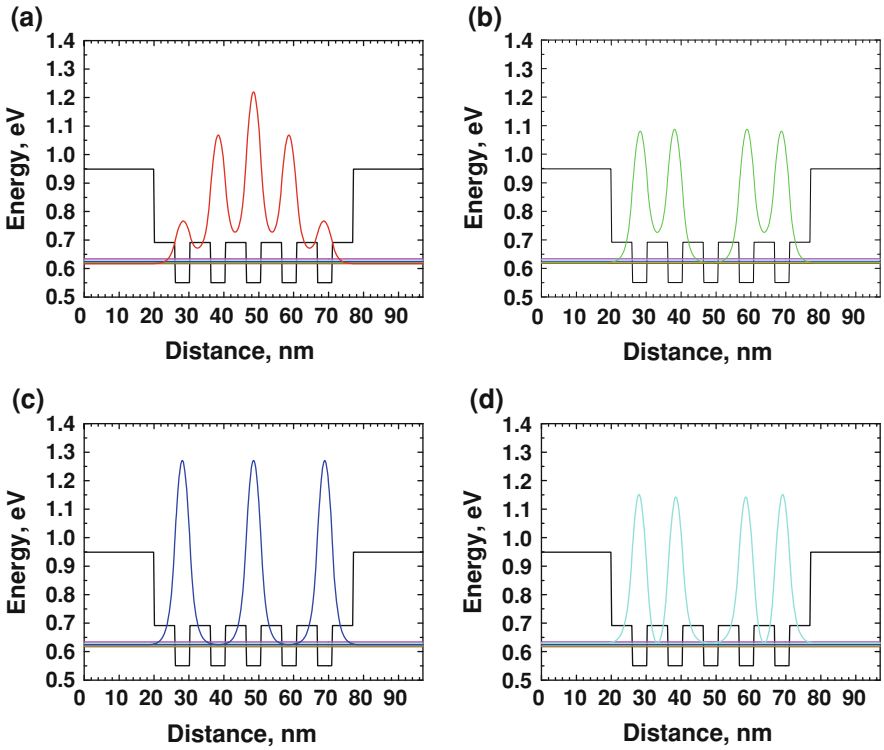

Fig. 2.24 Energy levels and the corresponding wave functions for the first four electron states in the conduction band in the active region

to the band gap temperature dependence, the perfect matching of the peak gain and the cavity wavelengths would take place at ~360 K, as can be obtained from the Fig. 2.26. This corresponds to the internal laser temperature of ~90°C, which will be achieved at outer temperatures in the range of 40–50°C. This enables stable laser operation in the whole desired temperature range, from 20°C up to 85–100°C.

Using quantum mechanical methods, e.g. effective mass theory and 8-band k*p theory, energy levels and wave functions in the QWs can be easily calculated. Consequently, temperature dependent emission wavelength of the active region can be efficiently designed. This information is inalienable for a correct VCSEL operation. But additionally to the internal electrical properties of the laser external limitations should be carefully considered. This includes electrical parasitics inside of the VCSEL as well as a proper design of the high frequency contact pads. Both of these effects should be designed to enable high speed VCSEL operation at desired data rates, which were for this work as high as 35–40 Gbit/s. These subjects will be considered in the next two sections.

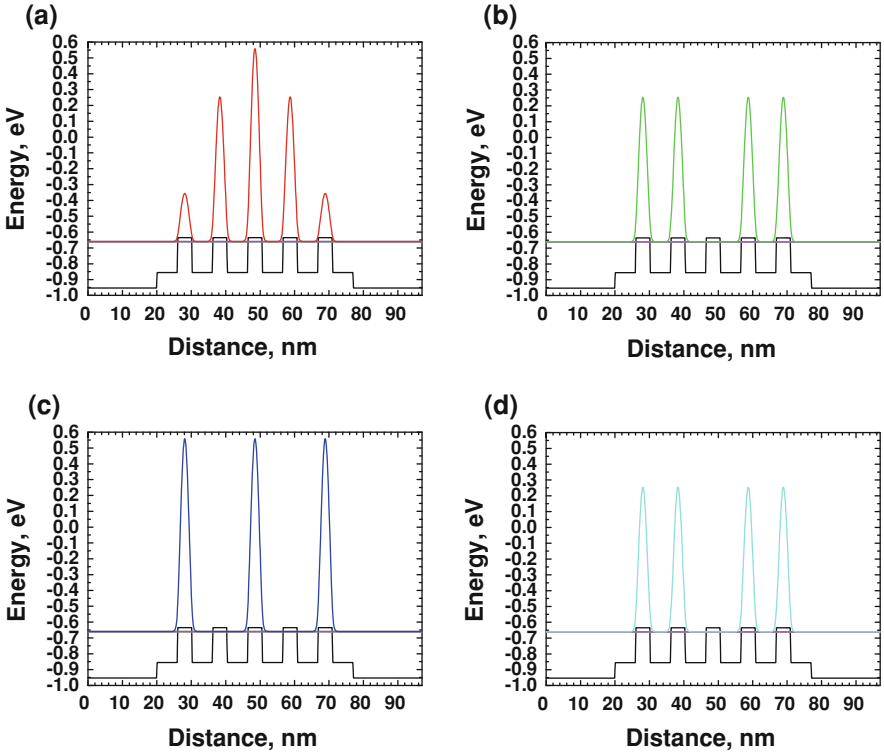

Fig. 2.25 Energy levels and the corresponding wave functions for the first four hole states in the heavy-hole band in the active region

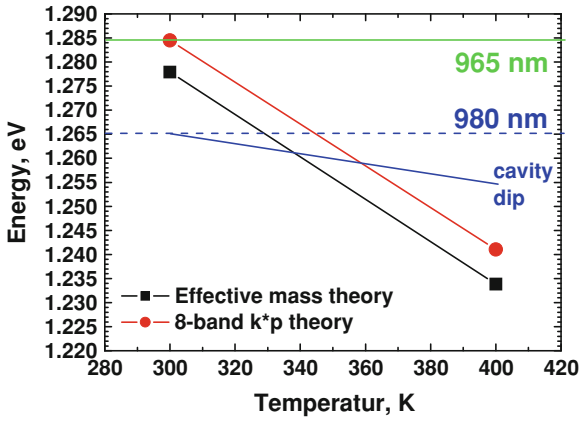

Fig. 2.26 Energy difference between the ground electron and hole levels as a function of the temperature, calculated with the effective mass theory and 8-band k*p theory, together with the goal wavelength of the active region peak emission at room temperature of 965 nm (*green line*), wavelength of the room temperature VCSEL emission at 980 nm (*blue dotted line*) and the temperature dependent cavity dip wavelength (*blue solid line*)

2.2.4 Equivalent Circuit and Electrical Parasitics of a VCSEL

For a proper operation of a semiconductor laser at high bit rates, high speed electrical current modulation driving the VCSEL should be transferred to the active region, where electro-optical conversion takes place, ideally without any distortions and attenuations. In a real VCSEL many effects prevent this. One of the most important of them is the presence of electrical parasitic elements, like unwanted capacitances and resistances, inside of the device, which build a low pass for the incoming high frequency electrical signal [38–41]. The exact form of the present electrical parasitic elements is determined first by the epitaxial structure, among other by doping levels, thickness and number of the oxide apertures etc., but also by the device design parameters chosen for fabrication, e.g. mesa size, oxide aperture diameter etc. That is why appropriate device design is of a great importance additionally to a proper epitaxial structure. In Fig. 2.27, a schematic picture of the electrical parasitic capacitances and resistances presented in a VCSEL is shown.

As one can see from Fig. 2.27a, additional to the resistance R_a and capacitance C_j, which represent the pumped active region, capacitance of the oxide aperture and the underlying intrinsic region C_o and of the contact pads C_p, as well as both resistances of the top and of the bottom DBR mirror R_{mt} and R_{mb}, should be considered. Since the two capacitances C_o and C_j are connected in parallel, they can be combined to one resistance C_a. According to the n-port theory [42], also both mirror resistances R_{mt} and R_{mb} together with eventually considerable contact resistances (not shown in the figure) can be represented by one common resistance R_m. By the given geometrical and structural parameters of a VCSEL all parasitic elements are defined and can be estimated using appropriate measurement techniques, for example S-parameter measurements [42].

The theory describing electrical high frequency properties of common network elements is the well known n-port theory [42]. Each port has two connections, and for VCSEL characterization the 2-port theory can be applied. The 2-port, describing the electrical parasitics in a VCSEL, is shown in Fig. 2.27b and is

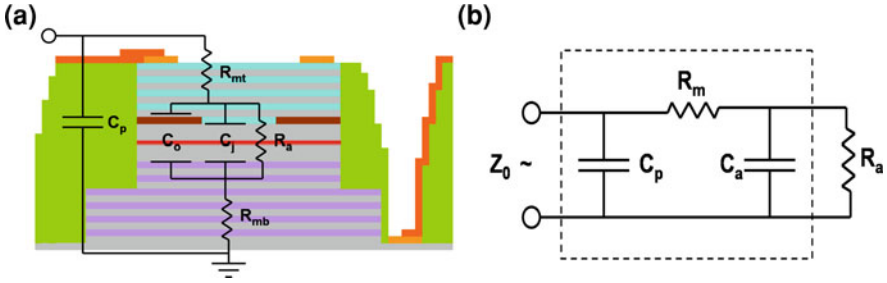

Fig. 2.27 Electrical parasitic capacitances and resistances inside a VCSEL (**a**) and the corresponding equivalent circuit with two parallel capacitances C_o and C_j combined together to C_a and resistances of the both mirrors R_{mt} and R_{mb} joined to R_m (**b**)

pointed by the dashed box. The first port connects a high frequency driving signal generator with impedance Z_0, commonly equal to 50 Ω, with the contact pads of the VCSEL. The second port describes the interface between electrical parasitics and the active region with the resistance R_a, which is the final destination of the incoming high frequency signal. All distortions and attenuations of the electrical signal within the dashed box are undesirable.

In Fig. 2.28 a common 2-port is shown. We describe the two ports symmetrically, so that a_i represents the incoming and b_i the outgoing signal for each port i. Z_i are reference impedances, which can be chosen free, but in the most cases it is comfortable to chose Z_1 to be equal to the generator (or driver) output impedance (commonly 50 Ω) and for Z_2 to use the resistance of the active region R_a of the desired VCSEL.

A 2-port can contain many elements, but its high frequency behavior is complete described by a 2 × 2 matrix, connecting the input and output signal magnitudes and phases. Hereby one can chose between several representations, which are free convertible. The most frequently used matrix is the S-matrix, or the so-called scattering matrix. The S-matrix handles not the voltage u_i and the current i_i at each port, but the forward propagating a_i and the backward propagating b_i waves. Forwards represents in this case the direction to the port and backwards the opposite direction. These waves for the two ports are shown in Fig. 2.28. The waves a_i and b_i are directly connected to the voltages u_i and currents i_i at the corresponding ports via the reference impedances Z_i, which are commonly real:

$$a_i = \frac{1}{2}\left(\frac{u_i}{\sqrt{Z_i}} + i_i\sqrt{Z_i}\right), \tag{2.2.27}$$

$$b_i = \frac{1}{2}\left(\frac{u_i}{\sqrt{Z_i}} - i_i\sqrt{Z_i}\right). \tag{2.2.28}$$

Corresponding voltages and currents on each port can be easily calculated from the a_i and b_i waves by using the reverse equations:

$$u_i = (a_i + b_i)\sqrt{Z_i}, \tag{2.2.29}$$

$$i_i = \frac{(a_i - b_i)}{\sqrt{Z_i}}. \tag{2.2.30}$$

Knowing the 2-port structure one can calculate the S-matrix, which connects the incoming and reflected waves to each other:

Fig. 2.28 A common 2-port with the symmetrical port notation

$$\begin{pmatrix} b_1 \\ b_2 \end{pmatrix} = S \cdot \begin{pmatrix} a_1 \\ a_2 \end{pmatrix} = \begin{pmatrix} S_{11} & S_{12} \\ S_{21} & S_{22} \end{pmatrix} \begin{pmatrix} a_1 \\ a_2 \end{pmatrix}. \tag{2.2.31}$$

The S-matrix includes additional to the parameters of the electrical elements of the 2-port also the reference impedances Z_i, that means it depends on some outer parameters, like generator impedance etc. There are several other matrices used in the 2-port, or more common n-port, theory, which depend only on the parameters of the electrical elements building the n-port, e.g. capacitances or resistances. The often used matrix is the Z-matrix, which handles again the voltages and currents instead of the a_i and b_i waves:

$$\begin{pmatrix} u_1 \\ u_2 \end{pmatrix} = Z \cdot \begin{pmatrix} i_1 \\ i_2 \end{pmatrix} = \begin{pmatrix} Z_{11} & Z_{12} \\ Z_{21} & Z_{22} \end{pmatrix} \begin{pmatrix} i_1 \\ i_2 \end{pmatrix}. \tag{2.2.32}$$

Both matrices are related by the following formula:

$$S = E - 2 \cdot (Z_N + E)^{-1}, \tag{2.2.33}$$

where E is the unit matrix and the matrix Z_N in the case of the 2-port is given by

$$Z_N = \begin{pmatrix} \frac{Z_{11}}{\sqrt{Z_1}\sqrt{Z_1}} & \frac{Z_{12}}{\sqrt{Z_1}\sqrt{Z_2}} \\ \frac{Z_{21}}{\sqrt{Z_2}\sqrt{Z_1}} & \frac{Z_{22}}{\sqrt{Z_2}\sqrt{Z_2}} \end{pmatrix}, \tag{2.2.34}$$

where Z_1 and Z_2 are the reference impedances.

With a network analyzer S-matrix of a 2-port can be easily measured. Since the second port of a VCSEL representing the active region is not achievable for a direct connection, only the S_{11} parameter can be investigated. That means that electrical parasitics of a VCSEL should be characterized based only on the measurement of electrical reflection of the incoming signal. That is why the 2-port describing the electrical parasitics of a VCSEL can not be determined from the incomplete S-matrix measurement, and some assumptions about the form of the parasitics should be met. In the most cases electrical parasitics of an oxide-confined VCSEL can be described by the equivalent circuit shown in Fig. 2.27b. This 2-port has three passive elements, two of which have the well known frequency dependence and R_m is frequency independent. The Z-matrix of this 2-port can be easily written and has the form

$$Z = \begin{pmatrix} \frac{R_1 \cdot (R_2 + R_3)}{R_1 + R_2 + R_3} & \frac{R_1 \cdot R_3}{R_1 + R_2 + R_3} \\ \frac{R_1 \cdot R_3}{R_1 + R_2 + R_3} & \frac{R_3 \cdot (R_1 + R_2)}{R_1 + R_2 + R_3} \end{pmatrix}, \tag{2.2.35}$$

with R_1, R_2 and R_3 defined as follows:

$$R_1 = -\frac{j}{2\pi C_p}, \tag{2.2.36}$$

$$R_2 = R_m, \tag{2.2.37}$$

$$R_3 = -\frac{j}{2\pi C_a}, \tag{2.2.38}$$

where j is the imaginary unit. Then using Eqs. 2.2.33 and 2.2.34 the S-matrix can be calculated setting Z_1 equal to 50 Ω and Z_2 equal to the resistance of the active region R_a. The calculated S_{11} can then be fitted to the measured real and imaginary parts of S_{11} and thus the four unknowns C_p, R_m, C_a and R_a can be estimated under the assumption that the used equivalent circuit represents electrical parasitics of the VCSEL correctly. Also more complicated n-ports can be simulated using advanced software, for example Microwave Office [43]. This gives the possibility to access individual parasitic elements directly and thus to analyze the electrical parasitics of VCSELs more efficiently. The frequency dependent S-parameter measurements up to 40 GHz were widely applied in the present work for VCSEL characterization and have helped to drastically improve the VCSEL performance.

2.2.5 *Design of Impedance Matched High Frequency Contact Pads*

After the VCSEL electrical parasitics have been considered in the previous section, in this section another important design issue will be described. In order to be able to guide the high frequency electrical driving signal to the VCSEL device, the laser should be equipped with appropriate contact pads, which should enable VCSEL operation at high frequencies. Since contact pads consist on high conductive metals, e.g. gold, chrome or platinum, the main problem to solve is not the attenuation of the signal but the impedance matching to the VCSEL driver or signal generator, which commonly have output standard impedances of 50 Ω. Thus contact pads should function at the same time as a high frequency transmission line. Free software for transmission line simulations is available, for example AppCAD [44] or TX Line [45], and in this work both AppCAD and TX Line were applied, delivering very similar results. In the following simulations carried out with TX Line for high speed contact pads designing will be presented.

There are different types of high speed transmission lines. Commonly, for VCSELs the so-called ground-signal-ground (GSG) transmission line is applied. Figure 2.29 shows schematically the GSG line with appropriate design parameters.

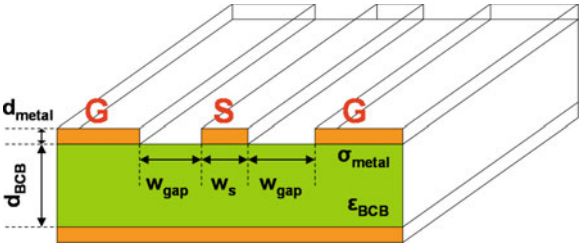

Fig. 2.29 Schematic view of a GSG transmission line with the corresponding parameters

A GSG transmission line consist of three metal lines: one for signal and two for the ground, which are placed symmetrically to the signal line and theoretically have infinite widths. The main design parameters are the width of the signal line w_s, the width of the gap between the signal and each ground line w_{gap}, the thickness of the dielectric, which was in our case bisbenzocyclobutene (BCB) d_{BCB} and the thickness of the applied metal d_{metal}. Also the dielectric constant of BCB ε_{BCB} and the metal conductivity σ_{metal} play an important role. All parameters were assumed to be frequency independent. Since all VCSELs investigated in this work were grown on doped semiconductor substrates, a GSG line having conductive material on the back side was simulated. Figure 2.30 shows simulation results for 5, 10 and 20 GHz with the corresponding parameters, which were used for VCSEL mask design for all VCSELs presented in this work.

From the figure one can see only weak frequency dependence of the transmission line impedance, which stays close to the goal impedance of 50 Ω received by using the parameters shown in the figure in red. Very important is the stability of the impedance to the variations of the design parameters, since these parameters can change during the fabrication process. Main reasons for this are limited precisions and reproducibility of the lithography steps but also of such important device fabrication techniques like metal deposition and BCB process. That is why the GSG-line should be designed in a way, that certain parameter changes would not drastically affect the transmission line impedance. In Fig. 2.31 simulation results for variations of all parameters and their effect on the transmission line impedance are presented.

From the figure one can see that the transmission impedance is very stable to design parameter changes. In a very wide variation range the impedance does not differ from the goal value of 50 Ω by more than 20%. For a better comparison the vertical impedance axis scaling is the same for all figures in Figs. 2.30 and 2.31.

After our investigations in this and also in the several previous sections we have seen, that electrical design of both epitaxial VCSEL structure, including the design of the active region, and also of the fabricated device is very important for a proper laser operation. Although, the physical processes, which should be considered

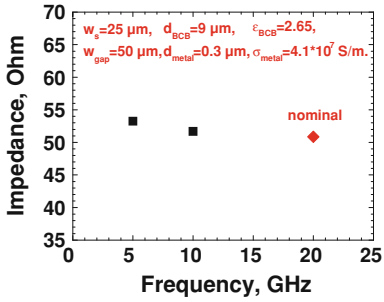

Fig. 2.30 Impedance for 5, 10 and 20 GHz with the corresponding nominal GSG-line parameters (*red*)

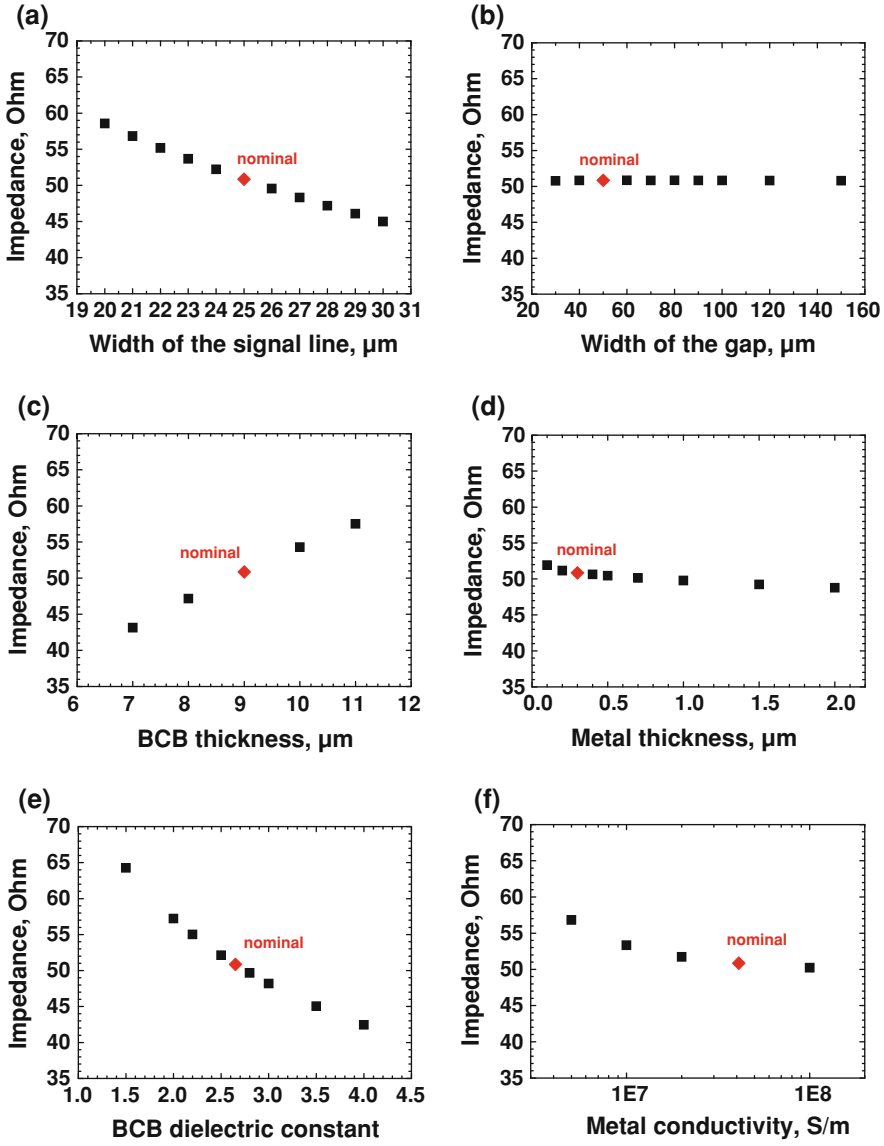

Fig. 2.31 Effects of the parameter variations on the transmission line impedance

during the VCSEL designing, are very complex, relatively simple methods could be applied in order to be able to solve all the design issues efficiently.

Optical and electrical phenomena build the basis of any semiconductor laser physics. Nevertheless each of them is affected in a very strongly manner by one physical quantity—the temperature. Temperature phenomena will be the main topic of the next section.

2.3 Thermal Properties

For a proper laser operation, not only at higher outer temperatures but also at room temperature, carefully designed thermal properties of the device are of the great importance, since the internal temperatures inside of the laser can be much higher than the ambience temperature. If semiconductor lasers operating at high outer temperatures, e.g. 85°C or higher, should be realized, thermal phenomena inside of the device become one of the crucial laser design aspects. It is of great importance to have a deeper understanding of the thermal processes in a laser, to know the heat generation and heat dissipation mechanisms. Because of the energy conservation, the part of the supplied electrical energy, which is not converted to optical energy inside of a laser, will generate heat in the device, strongly affecting device performance. Since efficiencies for converting electrical to optical power in common VCSELs are lower than 50%, the most part of the electrical energy introduced into the device will generate heat. The two major tasks of VCSEL thermal designing are to reduce the heat generation inside of the device and to carry off the heat, which have been generated, efficiently. Of course, it is better not to have the heat at all or to have only a small amount of it, than to generate much heat and to try to carry it off. In order to reduce heat generation, corresponding mechanisms should be studied. In a practical device a significant amount of the heat will be commonly still present, so heat flux phenomena should be considered as well. These mechanisms will be described in the present section.

2.3.1 Heat Generation and Thermal Resistance of Oxide-Confined VCSELs

Heat is generated in a semiconductor by transferring a part of the carrier energy to the lattice. These energy transfer processes are quantized and commonly described using quasi-particles called phonons, which then take part in heat dissipation processes. In the case of a local thermal equilibrium between lattice and carriers the heat flux is controlled by the temperature gradient [35]:

$$\vec{J}_{\text{Heat}} = -\kappa_L \vec{\nabla} T, \tag{2.3.1}$$

where $\vec{J}_{\text{Heat}}$ is the heat flux density (heat energy flux perpendicular to a unit surface), T is the local temperature and κ_L is the lattice thermal conductivity. In principle, electrons and holes contribute to the thermal conductivity, but their contribution is commonly small. The temperature should satisfy the heat flux equation

$$\rho_L C_L \frac{\partial T}{\partial t} = -\vec{\nabla} \cdot \vec{J}_{\text{Heat}} + H_{\text{Heat}}, \tag{2.3.2}$$

where ρ_L is the density of the semiconductor material, C_L is the lattice specific heat and $H_{\text{Heat}}(\vec{r},t)$ is the generated heat power density from various sources. All parameters in 2.3.2 are in a common case temperature dependent by itself. If temperature changes are comparable small, these parameters can be approximately handled as corresponding constants. In principle, from the two Eqs. 2.3.1 and 2.3.2, by defined boundary conditions and heat generation function H_{Heat}, the two unknowns T and $\vec{J}_{\text{Heat}}$ can be calculated.

In the static case the left hand side of (2.3.2) becomes zero and the heat flux is controlled only by one material constant, which is the thermal conductivity κ_L. The material of interest for the 850 and 980 nm VCSELs is $Al_xGa_{1-x}As$, which is a ternary alloy. Because of the random distribution of alloy atoms, which causes strong allow scattering of phonons, the thermal conductivity of ternary and quaternary alloys is significant reduced as compared to pure binary materials like GaAs or AlAs. A good estimation of the thermal conductivity of an alloy of the form AB_xC_{1-x} can be found using the equation

$$\frac{1}{\kappa_L(x)} = \frac{x}{\kappa_{AB}} + \frac{1-x}{\kappa_{BC}} + x(1-x)\cdot C_{ABC}, \tag{2.3.3}$$

where κ_{AB} and κ_{BC} are thermal conductivities of the corresponding binary materials and C_{ABC} is the corresponding empirical bowing parameter. Figure 2.32 shows the thermal conductivity of $Al_xGa_{1-x}As$ alloy calculated using Eq. 2.3.3 with corresponding material parameters [35] also shown in the picture.

As one can see the thermal conductivity goes down very fats with Al composition x and is already by 10% Al in AlGaAs reduced by more than a factor of two compared to pure binary GaAs. That is why using binary compounds are much more preferable from the point of view of the thermal properties of the lasers. Unfortunately at the wavelength of 850 nm pure GaAs is absorbing. That is why for the VCSELs emitting at this wavelength, like for the 850 nm QW-VCSELs

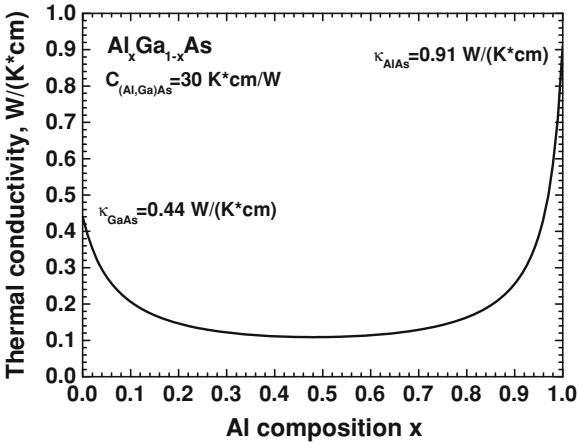

Fig. 2.32 Thermal conductivity of $Al_xGa_{1-x}As$ as a function of the Al composition x, calculated using Eq. 2.3.3; corresponding parameters are also shown

presented in this work, some amount of Al should be used, for example 15%. For 980 nm pure GaAs can be applied, but there is another important limitation, which is the growth technique used for VCSEL growth. In the case of MOCVD binary GaAs is commonly grown at different temperatures as $Al_xGa_{1-x}As$ alloy, so that from the practical point of view it is easier to use also at the wavelength of 980 nm the ternary $Al_xGa_{1-x}As$ alloy. In the 980 nm QW-VCSELs investigated in this work 12% Al was used. By using MBE for the VCSEL structure growth binary GaAs can be easily applied. This was made for the 980 nm SML-VCSELs investigated in the present work.

From the other side, binary AlAs has an even higher thermal conductivity as the binary GaAs and would be preferable to use, especially in the top DBR mirror. The limiting factor here is in the case of oxide-confined VCSELs the oxidation rate of $Al_xGa_{1-x}As$, which is strongly dependent on the Al composition. Since the oxidation is carried out after the mesa etch, $Al_xGa_{1-x}As$ layers used in the DBR mirrors will also oxidize, and in order to keep the oxidation rate small lower Al composition as compared to the aperture layer should be used. Commonly 98–100% of Al is applied for the aperture layers, so that for the DBR layers the Al composition should be in the range of 90% or lower. In all VCSEL presented in this work 90% of Al in both DBR mirrors were applied.

To understand and effectively reduce the heat generation, corresponding phenomena should be considered. In a semiconductor laser heat is generated by different mechanisms. The most relevant are the Joule heat, the electron–hole recombination heat, the Thomson heat and the heat from optical absorption.

The Joule heat is generated by the carrier flow through a semiconductor and the corresponding scattering by phonons. The heat generation is then written by [35]

$$H_J = \frac{\vec{j}_n^2}{q\mu n} + \frac{\vec{j}_p^2}{q\mu p}, \tag{2.3.4}$$

which is directly proportional to the electrical resistance of the material.

The recombination heat is generated by nonradiative recombination processes of the electron–hole pairs. These processes include defect and impurity recombination, recombination on surfaces and interfaces and Auger recombination. The average recombination heat is proportional to the difference between the quasi-Fermi levels:

$$H_R = R\left(F_n - F_p\right), \tag{2.3.5}$$

where R is the total recombination rate of the considered processes. One could include also the spontaneous recombination, since most of the emitted photons are absorbed by the semiconductor and eventually converted into heat.

The Thomson heat results from the differences in the thermoelectric power, which is the measure for the increase in average carrier excess energy with increasing temperature. A dramatic example is the interface between different semiconductors, like in a DBR mirror. By moving through an interface from a

material with the larger band gap to a material with the smaller band gap, electrons exhibit excess kinetic energy (hot electrons), which can dissipate to the lattice. In the opposite case electrons needs to receive some energy from the lattice. Thus the Thomson heat can be both positive and negative and is described by

$$H_T = -qT\left(\vec{j}_n \cdot \vec{\nabla} P_n + \vec{j}_p \cdot \vec{\nabla} P_p\right), \tag{2.3.6}$$

where P_n and P_p are the thermoelectric power for electrons and holes, respectively. Sometimes Thompson heat is also referred to as Peltier heat.

The optical absorption heat arises from the absorption of photons in the semiconductor material. Photons can be directly absorbed by the crystal lattice, but at the typical photon energies considered here the free carrier absorption is dominating. The absorbed energy is then quickly dissipated to the lattice due to very short intraband scattering times. The absorption heat is given by

$$H_A = \alpha \Phi h\nu, \tag{2.3.7}$$

where $\alpha(h\nu)$ is the wavelength dependent absorption coefficient, ν is the photon frequency and Φ is the photon flux energy, which can be calculated from the optical simulations considered above.

By setting together all heat generation mechanisms described by Eqs. 2.3.4–2.3.7 one can calculate the total heat generation rate H_{Heat} and use it for simulations of the thermal properties according to Eqs. 2.3.1 and 2.3.2.

An important quantity characterizing thermal properties of a VCSEL is its thermal resistance. If the heat power is generated mostly within one region, e.g. the active region in a VCSEL, the temperature increase in this region will be determined by the thermal resistance of the whole device and the generated heat power

$$\Delta T = R_{\text{th}} P_{\text{Heat}}, \tag{2.3.8}$$

where ΔT is the temperature difference between the heat source (commonly active region) and the heat sink, P_{Heat} is the total heat power and R_{th} is the thermal resistance of the laser. The heat power is equal to the supplied electrical power minus the output optical power:

$$P_{\text{Heat}} = UI - P_{\text{out}}, \tag{2.3.9}$$

where U and I are the operating laser voltage and current and P_{out} is the total optical output power. The thermal resistance of a VCSEL can be easily estimated by measuring the shift of the wavelength first with the current, additionally to the L-U-I-characteristics, at one temperature and then near the threshold for several higher temperatures. From the first measurement set the wavelength shift in dependence on the heat power can be calculated, while form the second measurement set the wavelength shift as a function of the temperature is directly measured. Combining the results of both sets, temperature increase as a function of the dissipated heat power and then according to (2.3.8) the thermal resistance can be calculated. Also the temperature of the active region can be directly measured

with this method. This enables to study and optimize high temperature laser performance more efficiently.

If one assumes the model of a uniform temperature disc, representing the active region of an oxide-confined VCSEL, on a homogeneous, isotropic, semi-infinite substrate, the thermal resistance can be given by the simple formula [46]:

$$R_{\text{th}} = \frac{1}{2\xi d}, \tag{2.3.10}$$

where ξ is the substrate thermal conductivity and d is the disc diameter. For a VCSEL, d corresponds to the effective pumped active region diameter, which is close to the aperture diameter. For ξ some effective value representing the bottom part of the cavity and the bottom DBR mirror should be used. If one assumes that the main heat source in the active region is the Joule heat, one can see from (2.3.4), that the heat power generated in the active region is directly proportional to the squared current flowing through it and the corresponding electrical resistance, mainly determined by the oxide aperture diameter d:

$$P_{\text{Heat}} = I_a^2 R_a = j_a^2 A^2 \rho_a \frac{l_a}{A} = j_a^2 \rho_a l_a \frac{\pi d^2}{4}, \tag{2.3.11}$$

where I_a is the current flowing through the active region, which in absence of large leakage currents is practically equal to the laser operation current I, j_a is the effective current density in the active region, A is the active region surface, R_a is the electrical resistance of the active region, ρ_a is the effective characteristic electrical resistance of the active region material and l_a is the active region effective length. If one then combines (2.3.8) and (2.3.10) using (2.3.11) one gets the following result for the temperature in the active region as a function of the aperture diameter:

$$\Delta T = \frac{1}{2\xi d} j_a^2 \rho_a l_a \frac{\pi d^2}{4} = C_{\text{eff}} j_a^2 d, \tag{2.3.12}$$

where C_{eff} represents all the constants describing the VCSEL structure and effectively independent on the current and aperture diameter:

$$C_{\text{eff}} = \frac{\rho_a l_a \pi}{8\xi}. \tag{2.3.13}$$

From Eq. 2.3.13 follows that for a constant current density in the active region j_a under described assumptions the temperature increase in VCSELs with larger aperture diameters d is larger as compared to VCSELs with smaller aperture diameters. This means that VCSELs with smaller apertures can operate at higher current densities at the same temperature as VCSELs with larger apertures.

2.3.2 Temperature Dependence of the Basic Laser Parameters

Since temperature affects practically each physical process in a semiconductor laser, it is inalienable to understand temperature dependence of the basic laser parameters. We will see in this section, that temperature effects have a very strong impact on laser operation not only at higher temperatures but also at room temperature, because, as we have seen in the previous section, the largest part of the introduced energy is converted to heat inside of a laser. This can be seen already for CW characteristics measured at room temperature, like L-I-curve and optical emission spectra. Figure 2.33 shows temperature dependent L-U-I characteristics and extracted values for the threshold current, maximum output power and maximum differential efficiency for temperatures from 20 to 100°C for an 850 nm QW-VCSEL.

One can see that device performance is strongly temperature dependent. The threshold current increases by more than twice for temperature changes between 20 and 100°C, the maximum output power decreases similarly and the differential efficiency drops also by more than 40%. But also at 20°C the output power does not stay a linear function, as predicted by the rate equation theory without temperature effects [1, 2]. The output power saturates at some point, called thermal roll-over, and then starts to decrease.

In order to understand temperature effects on laser operation qualitatively we should take a closer look on the laser equations. One of the most important characteristics of a semiconductor laser is its L-I-curve, this means its output power as a function of the driving current [1, 2]:

$$P_0 = \eta_d \frac{hv}{q}(I - I_{\text{th}}), \tag{2.3.14}$$

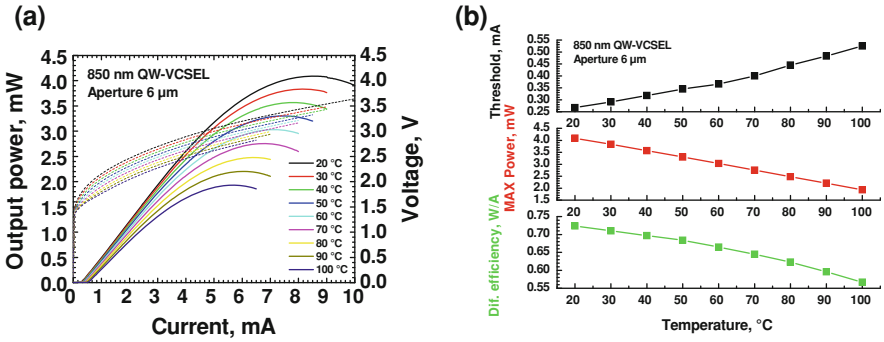

Fig. 2.33 Temperature dependent L-U-I characteristics (**a**) and extracted values for the threshold current, maximum output power and maximum differential efficiency (**b**) from 20 to 100°C for an 850 nm QW-VCSEL

where P_0 is the laser output power, η_d is the differential efficiency I is the driving current and I_{th} is the threshold current. The differential efficiency η_d can be expressed as follows:

$$\eta_d = \frac{\eta_i \alpha_m}{\alpha_i + \alpha_m}, \tag{2.3.15}$$

where η_i is the internal quantum efficiency or injection efficiency, which is the fraction of the terminal current that generates carrier in the active region, α_i is the internal or intrinsic cavity loss and α_m is the mirror loss, both already introduced in Eq. 2.1.23.

According to Eq. 2.3.14 the output power should be a linear function of the injected current. However, as one can see from Fig. 2.33, in the reality this is not the case even for one constant outer temperature. The reason is the internal heating, which increases the temperature inside of the device. The internal losses increase, approximately following the linear relationship $\alpha_i \propto T$ [2], which leads to a decrease of the differential efficiency according to (2.3.15). Exactly this experimentally measured behavior of the differential efficiency is shown in Fig. 2.33. Because the peak material gain for a given carrier density decreases, higher carrier densities are required to compensate increased losses and to achieve lasing. Accordingly the threshold current increases, which can be also seen in the Fig. 2.33.

The differential resistance of the laser commonly decreases with increasing temperature, because the conductivity of the semiconductor materials applied for laser fabrication increases. This can be seen also in the Fig. 2.33a, where the voltage at some constant defined current decreases with increasing temperature.

Finally the output power saturates at some internal temperature, because the incoming current can not compensate the increase of the threshold current and the drop of the differential efficiency any more. For VCSELs, important is the dependence of the roll-over current I_{ro} on the aperture diameter. If we assume that for any VCSEL from the same piece the thermal roll-over occurs at one defined temperature T_{ro}, we can easily derive the following dependence for a given outer or chuck temperature T_{chuck} using (2.3.8) and (2.3.10):

$$\Delta T_{\text{ro}} = T_{\text{ro}} - T_{\text{chuck}} = R_{\text{th}} I_{\text{ro}}^2 R_a = \frac{2\rho_a l_a}{\xi\pi} \frac{I_{\text{ro}}^2}{d^3}, \tag{2.3.16}$$

with already used in (2.3.11) electrical resistance of the active region R_a at the roll-over temperature, effective characteristic electrical resistance of the active region material ρ_a at the roll-over temperature and active region effective length l_a. Hereby d is the aperture diameter, if no current crowding is assumed, and ξ is the substrate thermal conductivity. We can rewrite Eq. 2.3.16 as follows:

$$I_{\text{ro}}^{2/3} = \sqrt{[3]}\frac{\xi\pi}{2\rho_a l_a} d = C_{\text{ro}} d. \tag{2.3.17}$$

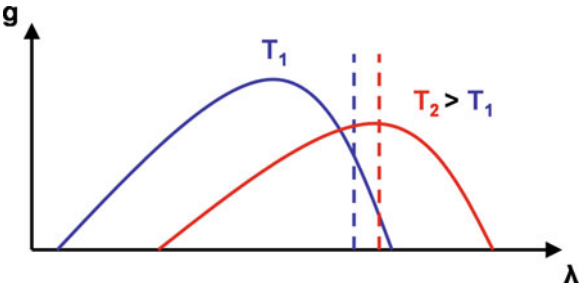

Fig. 2.34 Schematic illustration of changes in the cavity-gain detuning with increasing temperature; dashed lines show the wavelength of the cavity dip at both temperatures

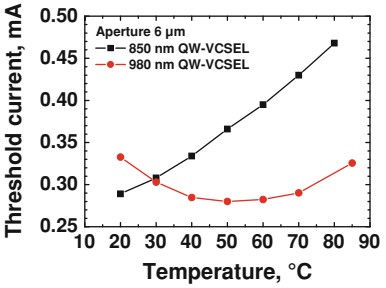

Fig. 2.35 Threshold current as function of temperature for a 850 nm QW-VCSEL and a 980 nm QW-VCSEL both with 6 μm aperture diameter

As one can see, the dependence of the roll-over current on the aperture diameter at a given outer temperature is not linear, but as one can see both experimentally and from Eq. 2.3.17 for larger apertures the roll-over current is also larger.

For VCSELs, where the lasing wavelength is defined not by the gain peak wavelength but by the cavity dip position, an additional important effect should be considered. This is the detuning between the cavity mode position and the peak gain. Because these both values have not identical temperature dependences, their difference changes with temperature. In Fig. 2.34 schematic illustration of this process is shown. As temperature increases, the gain peak commonly drops and shifts faster than the cavity dip, shown as dashed lines, so that the cavity-dip detuning decreases. It can happen that at a higher temperature more gain is available at the cavity wavelength, like in the schematic example shown in Fig. 2.34.

Knowing this one can design a VCSEL with the cavity-gain detuning optimized for a specific temperature. Figure 2.35 shows an example of such optimization.

In the figure threshold current for two VCSELs with nominally identical aperture diameter of 6 μm is shown. In the case of 850 nm QW-VCSEL the cavity-gain detuning was optimized for room temperature operation, while in the case of 980 nm QW-VCSEL optimal temperature was designed to be around 50°C. One can see, that the threshold current of the first VCSEL increases continuously with temperature, while for the 980 nm QW-VCSEL the threshold current decreases for temperatures up to 50°C, and then starts to increase, reaching at 85°C the value similar to 20°C. The overall changes are ~62% for the 850 nm

QW-VCSEL optimized for room temperature and only ∼19% for the 980 nm QW-VCSEL optimized for high temperature operation.

Temperature effects shortly described in this section play a major role and should be carefully considered during VCSEL designing process. Of course temperature affects not only CW characteristics of a laser. Also high frequency properties are affected in a very strongly manner. As we will see in further sections, one can efficiently design and fabricate high speed VCSELs operating at very high temperatures.

2.4 The Rate Equations

After optical, electrical and thermal properties of oxide-confined VCSELs were briefly investigated, in this section the temperature independent single-mode rate equation model will be described. This is a simple, but very powerful model, which describes dynamics of charge carriers and photons in a semiconductor laser [1, 2]. For the multimode case it has been demonstrated, both theoretically and experimentally, that index guided multimode VCSELs with highly overlapping transverse fields (such as oxide-confined VCSELs) have uniform carrier and photon densities and exhibit a single resonance frequency [47, 48], so that the single-mode rate equation model could be applied [49]. Because of its evidence and clearness the model is very helpful for understanding of the static and dynamic behavior of semiconductor lasers as well as for numerical qualitative and quantitative simulations of laser devices. By fitting model results to experimental data one gets access to important physical quantities describing a VCSEL, e.g. differential gain, relaxation resonance frequency, damping etc. Application of the rate equation model for analyzing real VCSELs is today a standard procedure for device understanding and improvement.

2.4.1 Rate Equation Model and Steady-State Solutions

In the rate equation model two types of particles play a role: charge carriers and photons. Because in mostly cases active region of a VCSEL is undoped or only lightly doped, under high injection levels, relevant for lasers, the charge neutrality requires the density of negative carriers (electrons) to be equal to the density of positive carriers (holes). In such cases one can investigate the density of only one type of carriers, for example of the electrons. This fact greatly simplifies the analysis.

In a semiconductor lasers there are several physical processes affecting dynamics of the carriers and photons. Figure 2.36 shows these processes used in the presented rate equation model. We will describe carriers and photons by their densities (expressed e.g. in units of $1/cm^3$): N for electrons and N_p for photons.

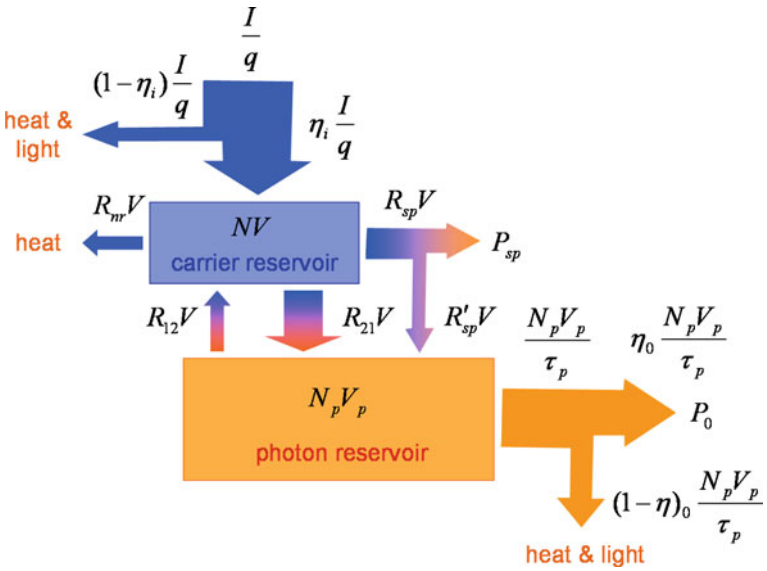

Fig. 2.36 Carrier and photon generation, recombination and transformation processes used in the rate equation model. *Blue arrows* correspond to carriers and *orange arrows* correspond to photons

The active region is hereby the region, where recombining carriers contribute to useful gain and photon emission, and corresponds in Fig. 2.36 to the carrier reservoir with the volume V. The photon reservoir is the lasing mode with an effective volume V_p, which is identical to the volume V_{eff} used in Eq. 2.1.44, and can be calculated as described in the previous sections. We will focus here on single-mode devices, but the rate equation theory can be easily adopted for the multimode case. In Fig. 2.36 for a better understanding the number of particles is shown, so that arrows describe the particle flow (particles per unit time, in units of e.g. 1/s), and boxes corresponds to the number of particles (which is dimensionless). If one summarizes all the processes shown in the figure, one arrives at the carrier and photon number rate equations:

$$V\frac{dN}{dt} = \frac{\eta_i I}{q} - \left(R_{\text{sp}} + R_{\text{nr}}\right)V - (R_{21} - R_{12})V, \tag{2.4.1}$$

$$V_p\frac{dN_p}{dt} = (R_{21} - R_{12})V - \frac{N_pV_p}{\tau_p} + R'_{\text{sp}}V. \tag{2.4.2}$$

Each term in (2.4.1) and (2.4.2) can be easily found in the Fig. 2.36. The number of carriers increases because of the first term on the right hand side in (2.4.1), which corresponds to the carrier injection by current. Here η_i is the internal quantum efficiency or injection efficiency, already introduced in (2.3.15), which is the fraction of the terminal current that generates carriers in the active region, and q is the magnitude of the electron charge. Spontaneous and non-radiative

recombination described by the spontaneous and non-radiative recombination rates R_{sp} and R_{nr} per unit volume and time, respectively, which have units of 1/(cm^3 s), are the major parasitic carrier loss mechanisms, that do not contribute noticeable to the photon density in the lasing mode. Finally, the last term in (2.4.1) describes the carrier loss (or generation) by the stimulated emission (or absorption) process. Hereby R_{21} is the stimulated emission rate per unite volume for photon emission into the lasing mode, and R_{12} is the stimulated absorption rate per unit volume for the photons from the lasing mode.

The last term of the (2.4.1) appears again on the right hand side of the (2.4.2), but this time it corresponds not to the loss of the carriers but to the increase of the photon number in the lasing mode. Another term describing the photon increase is the last term on the right hand side of (2.4.2), which corresponds to the part of photons generated by spontaneous emission, which goes into the lasing mode. Thereby R'_{sp} is the rate per unit volume of spontaneous emission into the lasing mode and can be described by the following equation:

$$R'_{sp} = \beta_{sp} R_{sp}, \tag{2.4.3}$$

where β_{sp} is the fraction of the photons generated by spontaneous emission, which goes into the lasing mode. In common VCSELs β_{sp} is in the order of 10^{-4}. By applying special cavity designs this value can be increased, leading to more efficient spontaneous recombination processes. Finally, the only term which corresponds to the photon losses is the second term on the right hand side of (2.4.2), which is dominated by the photon lifetime τ_p. The photon lifetime τ_p is given by

$$\frac{1}{\tau_p} = v_g(\alpha_m + \alpha_i) = \frac{\omega}{Q}, \tag{2.4.4}$$

where v_g is the group velocity of the mode of interest, including both material and waveguide dispersion, and α_m and α_i are the mirror and the spatial averaged internal cavity losses, already introduced in (2.1.23). Photon lifetime can be defined also in terms of the light frequency ω and the cavity quality factor Q, which sometimes can be advantageous. The mirror loss can be calculated using the optical properties of the cavity according to

$$\alpha_m = \frac{1}{2L} \ln\left(\frac{1}{R_1 R_2}\right), \tag{2.4.5}$$

where L is the effective cavity length and R_1 and R_2 are the power reflectivities of the top and bottom mirror in the case of VCSELs.

All recombination rates in (2.4.1) and (2.4.2) are dependent on the carrier density N. The non-radiative recombination rate R_{nr} can be expressed by

$$R_{nr} = AN + CN^3, \tag{2.4.6}$$

where constant coefficients A and C corresponds to different non-radiative recombination mechanisms, e.g. defect and impurity recombination, surface and

interface recombination and Auger recombination. In mostly VCSELs A could be assumed to be negligible. The constant C, describing the Auger recombination, is in the order of 10^{-29}–10^{-30} cm^6/s in the active regions used in common GaAs- and InGaAs-based VCSELs. The spontaneous emission rate R_{sp} has the following dependence on carrier density:

$$R_{sp} = BN^2, \tag{2.4.7}$$

where B is the bimolecular recombination coefficient and has a magnitude of $\sim 10^{10}$ cm^3/s for the most AlGaAs and InGaAsP alloys of interest.

The last term in (2.4.1), which is the first term on the right hand side of the (2.4.2), is the photon gain term and can be expressed using the following equation:

$$g = \frac{1}{N_p}\frac{dN_p}{dz} = \frac{1}{v_g N_p}\frac{dN_p}{dt} = \frac{1}{v_g N_p}(R_{21} - R_{12}), \tag{2.4.8}$$

where g is the material gain describing increase (or decrease, if negative) of the photon density N_p by passing through the active region. According to (2.4.8), the photon gain term in (2.4.1) and (2.4.2) can be expressed by

$$(R_{21} - R_{12}) = v_g g N_p. \tag{2.4.9}$$

The gain g is in a common case a function of both carrier and photon densities and can be approximated at a given wavelength by a logarithmic function

$$g(N, N_p) = \frac{g_0}{1 + \varepsilon N_p}\ln\left(\frac{N + N_s}{N_{tr} + N_s}\right), \tag{2.4.10}$$

where g_0, N_s and N_{tr} are constants and ε is the empiric gain compression factor, which is a constant as well.

One can rewrite (2.4.1) and (2.4.2) by dividing out the corresponding volumes and using the following equation:

$$\Gamma = \frac{V}{V_p}, \tag{2.4.11}$$

where Γ is the optical confinement factor already introduces in (2.1.23) and (2.1.45), and also using (2.4.9), to obtain the density rate equations, which are more familiar:

$$\frac{dN}{dt} = \frac{\eta_i I}{qV} - \left(R_{sp} + R_{nr}\right) - v_g g N_p, \tag{2.4.12}$$

$$\frac{dN_p}{dt} = \left(\Gamma v_g g - \frac{1}{\tau_p}\right)N_p + \Gamma R'_{sp}. \tag{2.4.13}$$

Putting (2.4.6) and (2.4.7) together and making the same with (2.4.4) and (2.4.5) we get

$$R_{\mathrm{sp}} + R_{\mathrm{nr}} = AN + BN^2 + CN^3, \tag{2.4.14}$$

$$\frac{1}{\tau_p} = v_g\left(\frac{1}{2L}\ln\left(\frac{1}{R_1R_2}\right) + \alpha_i\right). \tag{2.4.15}$$

Equations (2.4.12–2.4.15) together with (2.4.3) combined with (2.4.7), leading to Eq. 2.4.17, and also Eq. 2.4.10 which we will repeat here for more clearness as (2.4.16),

$$g\left(N, N_p\right) = \frac{g_0}{1 + \varepsilon N_p}\ln\left(\frac{N + N_s}{N_{tr} + N_s}\right), \tag{2.4.16}$$

$$R'_{\mathrm{sp}} = \beta_{\mathrm{sp}}R_{\mathrm{sp}} = \beta_{\mathrm{sp}}BN^2, \tag{2.4.17}$$

build the equation set (2.4.12–2.4.17) for the carrier density N and the photon density N_p, where all coefficients, excepted for the driving current I, are constants or can be expressed as functions of N and N_p. By solving this set of equations (2.4.12–2.4.17) one can investigate laser behavior under different types of current injection: constant current, small signal modulation, large signal modulation etc.

To get access to the output power of the lasing mode of interest, one can use the following equations:

$$P_0 = \eta_0 h\nu\frac{N_pV_p}{\tau_p}, \tag{2.4.18}$$

$$\eta_0 = F\frac{\alpha_m}{\alpha_m + \alpha_i}, \tag{2.4.19}$$

where η_0 is the optical efficiency, $h\nu$ is the photon energy and F is the fraction of power not reflected back into the cavity which escapes as useful power from the output coupling mirror. By multiplying the optical efficiency η_0 with the injection efficiency η_i one gets the differential efficiency η_d, defined earlier in (2.3.15), which can be easily measured experimentally:

$$\eta_d = \eta_i\eta_0. \tag{2.4.20}$$

The factor F is for common VCSELs close to 1, that is why it was suppressed in (2.3.15).

By setting the time derivatives for the carrier and photon density equal to zero in the equation set (2.4.12–2.4.17), one gets the steady-state equations describing laser behavior under constant current injection. The steady-state solution is

$$N_p = \frac{\Gamma R'_{\mathrm{sp}}}{1/\tau_p - \Gamma v_g g}, \tag{2.4.21}$$

$$I = \frac{qV}{\eta_i}\left(R_{\mathrm{sp}} + R_{\mathrm{nr}} + v_g g N_p\right). \tag{2.4.22}$$

Here one can use the carrier density N as the independent variable for more physical understanding. One can apply following equations

$$\Gamma v_g g_{\text{th}} \equiv \frac{1}{\tau_p}, \tag{2.4.23}$$

$$g(N_{\text{th}}) = g_{\text{th}}, \tag{2.4.24}$$

to define the threshold gain g_{th} and the corresponding threshold carrier density N_{th}. With this definitions one can solve for $v_g g N_p$ in (2.4.21) and by setting the result to (2.4.22) one gets the following expression for the current:

$$I = \frac{qV}{\eta_i}\big(\big(1-\beta_{\text{sp}}\big)R_{\text{sp}} + R_{\text{nr}} + v_g g_{\text{th}} N_p\big). \tag{2.4.25}$$

For the case when the laser is driven well above threshold, one can use threshold values by applying $N \to N_{\text{th}}$ for all parameters in (2.4.21) and (2.4.25) except for the g in the denominator of (2.4.21), leading to

$$N_p(N) = \frac{R'_{\text{sp}}(N_{\text{th}})/v_g}{g_{\text{th}} - g(N)}, \tag{2.4.26}$$

$$I = \frac{qV}{\eta_i}\big(\big(1-\beta_{\text{sp}}(N_{\text{th}})\big)R_{\text{sp}}(N_{\text{th}}) + R_{\text{nr}}(N_{\text{th}})\big) + \frac{qV}{\eta_i} v_g g_{\text{th}} N_p(N). \tag{2.4.27}$$

It is clear from (2.4.26) that the carrier density N and gain g actually never reach their threshold values N_{th} and g_{th} for finite output powers and currents. They remain ever below these values.

From (2.4.18) one can rewrite the output power using the definition (2.4.23) and (2.4.11) as follows:

$$P_0 = \eta_0 h\nu\big(V v_g g_{\text{th}} N_p\big). \tag{2.4.28}$$

By solving for $V v_g g_{\text{th}} N_p$ in (2.4.28) and putting the result into the last term of (2.4.27) one can get after some rearrangement the output power in the lasing mode P_0 as a function of the driving current I, the so-called L-I-curve:

$$P_0 = \eta_i \eta_0 \frac{h\nu}{q}(I - I_{\text{th}}), \tag{2.4.29}$$

where the threshold current I_{th} is defined by

$$I_{\text{th}} = \frac{qV}{\eta_i}\big(\big(1-\beta_{\text{sp}}(N_{\text{th}})\big)R_{\text{sp}}(N_{\text{th}}) + R_{\text{nr}}(N_{\text{th}})\big). \tag{2.4.30}$$

One can see from (2.4.29) that the output power in the lasing mode increases linearly with the injected current above threshold. The threshold current is determined according to (2.4.30) by the spontaneous and non-radiative recombination rates at the threshold carrier density N_{th}, which is defined by the mirror and

internal losses corresponding to (2.4.23) and (2.4.15) and by the form of the gain dependence on the carrier and photon densities (2.4.16). If the non-radiative recombination rate R_{nr} is negligible and $\beta_{sp} = 1$ the threshold current would be equal to zero and the so-called "thresholdless" laser would be realized. However, for typical lasers $\beta_{sp} \ll 1$ and the threshold current remains finite.

To illustrate the behavior of the carrier density, photon density, gain and output power during the laser steady-state operation, their dependence on the injected current is shown in Fig. 2.37.

As one can see from the figure, the photon density N_p and accordingly the output power in the lasing mode show a drastic increase as the injected current reaches its threshold value (denoted by the vertical line near 400 μA). Above threshold the photon density and the output power increase linearly with the current, as predicted by (2.4.27) and (2.4.29). The carrier density N and the gain g nearly saturate at threshold and increase at currents above threshold only by a small amount.

As one example of application of the rate equations one can take a look on the simulated L-I-curves for different values of the reflectivity of the top mirror of an oxide-confined VCSEL and also for different internal cavity losses, shown in Fig. 2.38. The first three L-I-curves correspond to the same value of internal losses α_i equal to 20 cm^{-1}, but to different top mirror reflectivities of 99.7, 99.6 and 99.5%. Accordingly to (2.4.23) and (2.4.15) the threshold gain increases with increased mirror losses (lower top mirror reflectivities) leading to an increase in the threshold current. The differential efficiency η_d, represented by the slope of the L-I-curves, increases as well, as predicted by (2.4.19) and (2.4.20).

A different situation exists if not the mirror losses α_m but the internal losses α_i are increased, as shown by the fourth L-I-curve in Fig. 2.38. Here again the threshold current increases, but the differential efficiency decreases, as can be easily seen from (2.4.19) and (2.4.20). Thus by investigating measured L-I-curves and applying results of the rate equation theory one can distinguish between different physical processes in a semiconductor laser. Numerical simulations

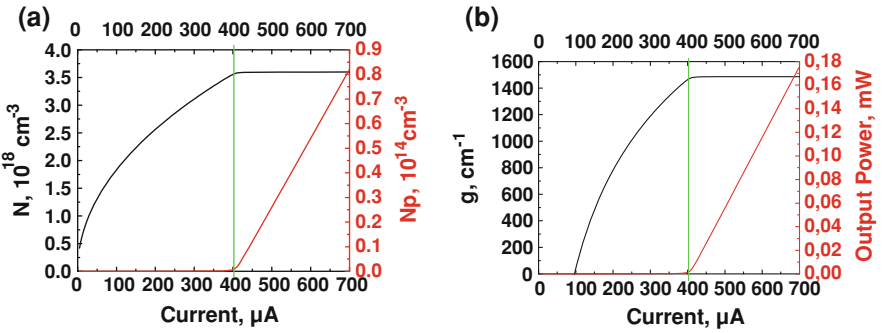

Fig. 2.37 Simulated carrier density N and photon density N_p (**a**) and gain g and output power (**b**) as a function of the injected current I; the *vertical line* denotes the position of the threshold current

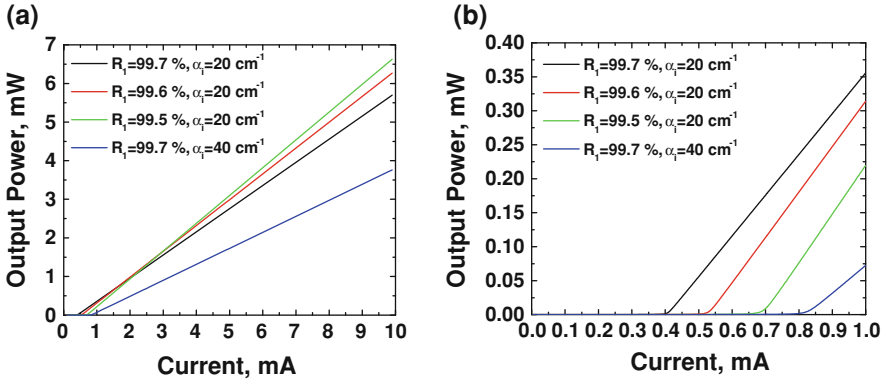

Fig. 2.38 Simulated L-I characteristics for VCSELs with different reflectivities of the top mirror and different internal cavity losses (**a**) and the zoomed view (**b**)

implementing rate equations are very useful for understanding of the physical processes inside of a semiconductor laser. Combined with a deeper analysis of the corresponding equations they provide a very powerful framework for successful VCSEL designing.

In this section rate equations were introduced without paying attention to temperature effects, that is why the simulated L-I-curves, e.g. those shown in Fig. 2.38, are strictly linear and do not behave similar to measured L-I-curves, e.g. those shown in Fig. 2.33. In principle one can add temperature effects by introducing temperature dependence for corresponding physical parameters.

Understanding of the principles of the laser operation under the constant current injection, i.e. in the CW regime, is an indispensable precondition for successful VCSEL development. Additionally, for high-speed VCSELs, like for those investigated in this work, modulation properties at high frequencies are the major issue to be understood and improved. That is why the next important application of the rate equations is the simulation of the semiconductor laser dynamics. This will be the topic of the next section.

2.4.2 Small-Signal Frequency Response

To be able to analyze dynamical behavior of semiconductor lasers one should consider the rate equations (2.4.12) and (2.4.13) with the time derivatives on the left hand side included. Unfortunately there is no analytical solution for this equation set, thus one must solve the equations numerically or apply some approximations to get analytical solutions. One of such approximations is the assumption that the changes in the carrier and photon densities away from their steady-state values are small compared to these steady-state densities. Then one can investigate the so-called small-signal responses of one variable in terms of

perturbation to another and get insight into the dynamic processes in the laser. For this purpose one can take differential of both (2.4.12) and (2.4.13), considering the injection current I, the carrier density N, the photon density N_p and the gain g as dynamic variables:

$$d\left[\frac{dN}{dt}\right] = \frac{\eta_i}{qV}dI - \frac{1}{\tau_{\Delta N}}dN - v_g g dN_p - N_p v_g dg, \tag{2.4.31}$$

$$d\left[\frac{dN_p}{dt}\right] = \left(\Gamma v_g g - \frac{1}{\tau_p}\right)dN_p + N_p \Gamma v_g dg + \frac{\Gamma}{\tau'_{\Delta N}}dN. \tag{2.4.32}$$

Hereby the differential carrier lifetime $\tau_{\Delta N}$ and the differential lifetime of carriers, which radiate photons into the lasing mode, $\tau'_{\Delta N}$ were introduced according to the following equations:

$$\frac{1}{\tau_{\Delta N}} = \frac{dR_{\mathrm{sp}}}{dN} + \frac{dR_{\mathrm{nr}}}{dN} = A + 2BN + 3CN^2, \tag{2.4.33}$$

$$\frac{1}{\tau'_{\Delta N}} = \frac{dR'_{\mathrm{sp}}}{dN} = 2\beta_{\mathrm{sp}}BN + \frac{d\beta_{\mathrm{sp}}}{dN}BN^2. \tag{2.4.34}$$

The differential carrier lifetime for the carriers emitting into the lasing mode $\tau'_{\Delta N}$ is typically in the range of tens of microseconds, and its contribution is negligible in the most cases.

One can expand the gain differential, paying attention to the fact that gain depends both on carrier and photon densities:

$$dg = a dN - a_p dN_p, \tag{2.4.35}$$

where the gain derivative regarding to the carrier density a and the negative gain derivative regarding to the photon density a_p were introduced. If one assumes the gain dependence like in (2.4.16), following equations for the gain derivatives will hold:

$$a = \frac{\partial g}{\partial N} = \frac{g_0}{(N + N_s)\left(1 + \varepsilon N_p\right)}, \tag{2.4.36}$$

$$a_p = -\frac{\partial g}{\partial N_p} = \frac{\varepsilon g}{\left(1 + \varepsilon N_p\right)}, \tag{2.4.37}$$

where both a and a_p are not constant but depend on carrier and photon densities. Inserting (2.4.35) into (2.4.31) and (2.4.32) and rearranging several terms one gets following equations, where only dI, dN and dN_p are present as independent differentials:

$$d\left[\frac{dN}{dt}\right] = \frac{\eta_i}{qV}dI - \left(\frac{1}{\tau_{\Delta N}} + N_p v_g a\right)dN - \left(v_g g - N_p v_g a_p\right)dN_p, \tag{2.4.38}$$

$$d\left[\frac{dN_p}{dt}\right] = \left(\frac{\Gamma}{\tau'_{\Delta N}} + N_p \Gamma v_g a\right) dN - \left(\frac{1}{\tau_p} - \Gamma v_g g + N_p \Gamma v_g a_p\right) dN_p. \tag{2.4.39}$$

One can eliminate also the gain by rearranging the steady-state equation (2.4.21), leading to

$$\frac{1}{\tau_p} - \Gamma v_g g = \frac{\Gamma R'_{\text{sp}}}{N_p}. \tag{2.4.40}$$

Applying (2.4.40) one can rewrite (2.4.38) and (2.4.39) in a more compact matrix form

$$\frac{d}{dt}\begin{bmatrix} dN \\ dN_p \end{bmatrix} = \begin{bmatrix} -\gamma_{NN} & -\gamma_{NP} \\ \gamma_{PN} & -\gamma_{PP} \end{bmatrix} \begin{bmatrix} dN \\ dN_p \end{bmatrix} + \frac{\eta_i}{qV} \begin{bmatrix} dI \\ 0 \end{bmatrix}, \tag{2.4.41}$$

with

$$\gamma_{NN} = \frac{1}{\tau_{\Delta N}} + v_g a N_p, \tag{2.4.42}$$

$$\gamma_{NP} = v_g g - v_g a_p N_p = \frac{1}{\Gamma \tau_p} - \frac{R'_{\text{sp}}}{N_p} - v_g a_p N_p, \tag{2.4.43}$$

$$\gamma_{PN} = \frac{\Gamma}{\tau'_{\Delta N}} + \Gamma v_g a N_p, \tag{2.4.44}$$

$$\gamma_{PP} = \frac{1}{\tau_p} - \Gamma v_g g + \Gamma v_g a_p N_p = \frac{\Gamma R'_{\text{sp}}}{N_p} + \Gamma v_g a_p N_p. \tag{2.4.45}$$

Well above threshold, where photon density N_p is large enough, one can suppress several terms in (2.4.42–2.4.45) leading to

$$\gamma_{NN} = \frac{1}{\tau_{\Delta N}} + v_g a N_p, \tag{2.4.46}$$

$$\gamma_{NP} = \frac{1}{\Gamma \tau_p} - v_g a_p N_p, \tag{2.4.47}$$

$$\gamma_{PN} = \Gamma v_g a N_p, \tag{2.4.48}$$

$$\gamma_{PP} = \Gamma v_g a_p N_p. \tag{2.4.49}$$

By investigating solutions of the equation set (2.4.41) one can get insight into the physical processes in a semiconductor laser under small-signal modulation. The coefficients (2.4.42–2.4.45) or (2.4.46–2.4.49) can be considered as constants. Although these coefficients depend on the carrier and photon densities N and N_p, these densities are determined at a certain working current I and can be extracted

by solving the equation set (2.4.12–2.4.17) for the steady-state case, as was described earlier.

Important are the small-signal responses to a sinusoidal current modulation dI. To solve (2.4.41) for this case, one can assume sinusoidal time dependence of all three small-signal variables dI, dN and dN_p:

$$dI(t) = I_1 e^{j\omega t}, \tag{2.4.50}$$

$$dN(t) = N_1 e^{j\omega t}, \tag{2.4.51}$$

$$dN_p(t) = N_{p1} e^{j\omega t}, \tag{2.4.52}$$

where I_1, N_1 and N_{p1} are constant complex amplitudes (including magnitude and phase) of the modulation current, carrier density and photon density, accordingly, and j is the complex unity. Introducing (2.4.50–2.4.52) into (2.4.41), and after some rearrangements one obtains the following equation set for the complex amplitudes N_1 and N_{p1}:

$$\begin{bmatrix} \gamma_{NN} + j\omega & \gamma_{NP} \\ -\gamma_{PN} & \gamma_{PP} + j\omega \end{bmatrix} \begin{bmatrix} N_1 \\ N_{p1} \end{bmatrix} = \frac{\eta_i I_1}{qV} \begin{bmatrix} 1 \\ 0 \end{bmatrix}. \tag{2.4.53}$$

To get the solutions one needs to obtain the determinant of the matrix from (2.4.53), which is given by

$$\Delta \equiv \begin{vmatrix} \gamma_{NN} + j\omega & \gamma_{NP} \\ -\gamma_{PN} & \gamma_{PP} + j\omega \end{vmatrix} = \gamma_{NP}\gamma_{PN} + \gamma_{NN}\gamma_{PP} - \omega^2 + j\omega(\gamma_{NN} + \gamma_{PP}). \tag{2.4.54}$$

The small-signal carrier and photon densities can be consequently written down as

$$N_1 = \frac{\eta_i I_1}{qV} \cdot \frac{\gamma_{PP} + j\omega}{\omega_R^2} \cdot H(\omega), \tag{2.4.55}$$

$$N_{p1} = \frac{\eta_i I_1}{qV} \cdot \frac{\gamma_{PN}}{\omega_R^2} \cdot H(\omega), \tag{2.4.56}$$

with the two-parameter modulation transfer function $H(\omega)$ given by

$$H(\omega) = \frac{\omega_R^2}{\Delta} \equiv \frac{\omega_R^2}{\omega_R^2 - \omega^2 + j\omega\gamma}. \tag{2.4.57}$$

Here the relaxation resonance frequency ω_R and the damping factor γ are defined as follows:

$$\omega_R^2 \equiv \gamma_{NP}\gamma_{PN} + \gamma_{NN}\gamma_{PP}, \tag{2.4.58}$$

$$\gamma \equiv \gamma_{NN} + \gamma_{PP}. \tag{2.4.59}$$

One can insert the coefficients (2.4.42–2.4.45) into (2.4.58) and (2.4.59) and make some rearrangements in order to get the relaxation resonance frequency and the damping factor in the terms of the laser parameters:

$$\omega_R^2 = \frac{N_p v_g a}{\tau_p} + \left(\frac{\Gamma N_p v_g a_p}{\tau_{\Delta N}} - \frac{\Gamma v_g g}{\tau_{\Delta N}}\right)\left(1 - \frac{\tau_{\Delta N}}{\tau'_{\Delta N}}\right) + \frac{1}{\tau_{\Delta N}\tau_p}, \tag{2.4.60}$$

$$\gamma = \left(\frac{1}{\tau_{\Delta N}} + N_p v_g a\right) + \left(\frac{1}{\tau_p} + \Gamma N_p v_g a_p\right) - \Gamma v_g g. \tag{2.4.61}$$

As one can see from the terms grouped together in (2.4.61), in the first bracket terms leading to losses in the carrier density caused by the changes in this carrier density itself are present. The second bracket represents terms, which lead to losses in the photon density caused by the changes in this photon density itself. Finally, the last term of this equation is the term corresponding to the increase of the photon density, caused by the changes in this photon density itself. In (2.4.60) many terms from (2.4.61) are present, but in a modified form, divided by the differential carrier lifetimes $\tau_{\Delta N}$ and $\tau'_{\Delta N}$ or photon lifetime τ_p. Eliminating gain with (2.4.40) one obtains

$$\omega_R^2 = \frac{v_g a N_p}{\tau_p} + \left(\frac{\Gamma v_g a_p N_p}{\tau_{\Delta N}} + \frac{\Gamma R'_{\mathrm{sp}}}{N_p \tau_{\Delta N}}\right)\left(1 - \frac{\tau_{\Delta N}}{\tau'_{\Delta N}}\right) + \frac{1}{\tau'_{\Delta N}\tau_p}, \tag{2.4.62}$$

$$\gamma = v_g a N_p \left(1 + \frac{\Gamma a_p}{a}\right) + \frac{1}{\tau_{\Delta N}} + \frac{\Gamma R'_{\mathrm{sp}}}{N_p}. \tag{2.4.63}$$

Equation 2.4.62 for the relaxation resonance frequency ω_R can be further simplified for the case that the laser operates well above threshold. In this case the first term will dominate and the relaxation resonance frequency can be expressed as

$$\omega_R^2 \approx \frac{v_g a N_p}{\tau_p}. \tag{2.4.64}$$

The damping factor γ (2.4.63) can be rewritten using (2.4.64) for the laser operation well above threshold to the following equation:

$$\gamma \approx K f_R^2 + \gamma_0, \tag{2.4.65}$$

where

$$f_R = \frac{\omega_R}{2\pi}, \tag{2.4.66}$$

and the K-factor K with the damping factor offset γ_0 are defined as follows:

$$K = 4\pi^2 \tau_p \left(1 + \frac{\Gamma a_p}{a}\right), \tag{2.4.67}$$

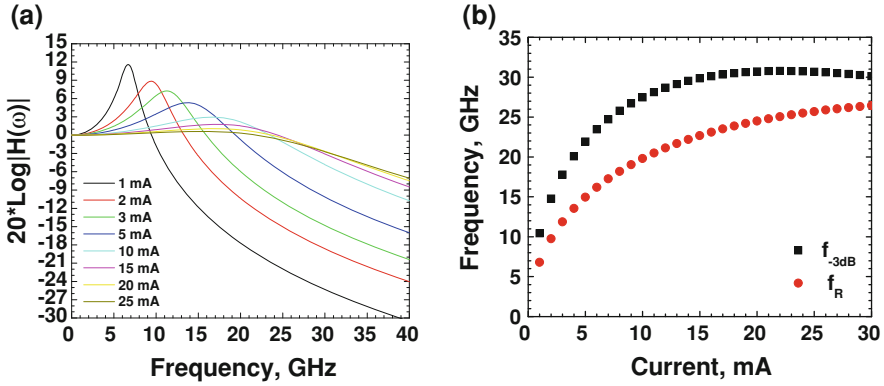

Fig. 2.39 Simulated modulation transfer functions for different currents (**a**) and corresponding relaxation resonance frequency and bandwidths (**b**) for an oxide-confined VCSEL

$$\gamma_0 = \frac{1}{\tau_{\Delta N}} + \frac{\Gamma R'_{\mathrm{sp}}}{N_p}. \tag{2.4.68}$$

In Fig. 2.39, a simulated modulation transfer functions for several different currents for an oxide-confined VCSEL according to (2.4.57) are shown.

The modulation transfer function can be expressed in decibels (dB). Because not the optical output power of the laser but rather the electrical power on the photodetector, which corresponds to the squared optical power, is relevant for applications, conversion to decibels is carried out using a factor of 20 rather than 10 before logarithm, as shown in the last term in the equation below:

$$H[\mathrm{dB}] = 10 * \log|\mathrm{H}|^2 = 20 * \log|\mathrm{H}|. \tag{2.4.69}$$

One can see from Fig. 2.39a that at low currents relaxation resonance is well-marked, but at higher currents it becomes damped because of the increased damping factor according to (2.4.65). The position of the relaxation resonance also shifts to larger frequencies at larger currents, which can be more clearly seen from the Fig. 2.39b, where corresponding values for the relaxation resonance frequency and bandwidth are shown. One can understand the shift of the relaxation resonance frequency with current by combining (2.4.18) with (2.4.29) and inserting it into (2.4.64), leading together with (2.4.66) to

$$f_R = \frac{1}{2\pi}\sqrt{\frac{\eta_i v_g a}{qV_p}} \cdot \sqrt{I - I_{\mathrm{th}}} = D\sqrt{I - I_{\mathrm{th}}}, \tag{2.4.70}$$

where the D-factor D, characterizing the slope of the relaxation resonance frequency with current, was introduced. The D-factor is in a common case not constant because of the dependence of the differential gain a on carrier and photon densities according to (2.4.36). At higher carrier and photon densities it becomes smaller leading to a weaker increase of the relaxation resonance frequency. Also

temperature effects, which were not considered in this section, play an important role. One defines empirically the corresponding modulation current efficiency factor M for the 3 dB-frequency $f_{\text{-3dB}}$, also called the bandwidth of the laser, which is the frequency, at which the modulation transfer function decreases by 3 dB compared to the starting point at zero frequency:

$$f_{-3\,\text{dB}} = M\sqrt{I - I_{\text{th}}}. \tag{2.4.71}$$

The linear increase of the relaxation resonance frequency f_R and of the 3 dB-frequency $f_{\text{-3dB}}$ with the square root of the current above threshold at lower currents is demonstrated in Fig. 2.40a, where corresponding values for an oxide-confined VCSEL are shown.

In Fig. 2.40b extracted dependence of the damping factor on the squared relaxation resonance frequency according to (2.4.65) is shown. Again, because the K-factor K (2.4.67) and the damping offset γ_0 (2.4.68) are commonly not constant but depend on carrier and photon densities, the linear relationship is not maintained over the whole range. At larger relaxation resonance frequencies, which correspond to larger operation currents and thus larger carrier and photon densities, both K and γ_0 increase, leading to a super linear dependence. Again thermal effects would play also here a very important role, making the trends more pronounced.

One can rewrite (2.4.65) using (2.4.70), which will lead to a linear relationship between the damping factor and the operation current:

$$\gamma \approx KD^2(I - I_{\text{th}}) + \gamma_0. \tag{2.4.72}$$

From the measurement point of view one can get access to the modulation transfer function H by measuring the modulation of the laser output power P_1, leaving the small modulation of the driving current I_1 constant and making the

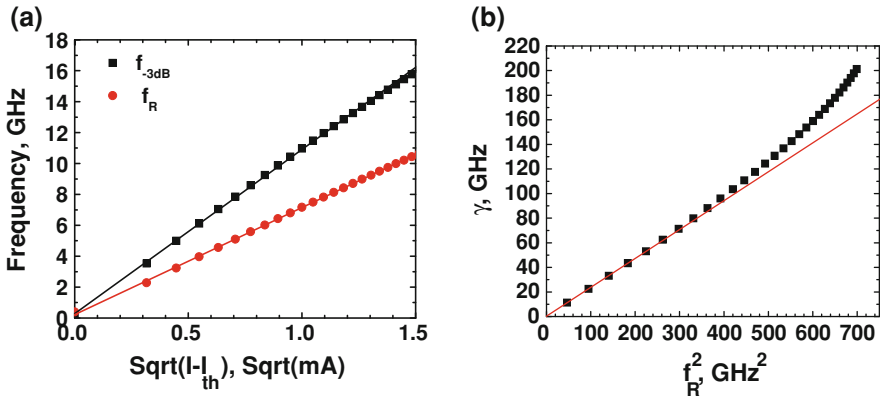

Fig. 2.40 Relaxation resonance frequency and 3 dB-frequency as functions of the square root of the current above threshold (**a**) and damping factor as a function of the squared relaxation resonance frequency (**b**) with corresponding linear fits for an oxide-confined VCSEL

frequency sweep. Using (2.4.56) together with (2.4.48) and (2.4.64) for the operation well above threshold one obtains

$$\frac{N_{p1}}{I_1} = \frac{\eta_i}{qV}\Gamma\tau_p H(\omega). \tag{2.4.73}$$

Now applying (2.4.18) and (2.4.11) one can expand (2.4.73) further to

$$\frac{P_1}{I_1} = \eta_i\eta_0\frac{h\nu}{q}H(\omega), \tag{2.4.74}$$

with the photon energy $h\nu$. As one can see from (2.4.74), the modulation transfer function can be measured experimentally, giving the possibility to get access to important laser parameters. Of course one should pay attention to other physical effects not considered in this section, e.g. thermal effects or electrical parasitics. For the latter one can introduce an additional term into (2.4.57), which, after some rearrangements, using (2.4.66) can be represented by

$$H(f) = \frac{f_R^2}{f_R^2 - f^2 + j\cdot f\cdot\frac{\gamma}{2\pi}}\cdot\frac{1}{1+j\cdot\frac{f}{f_p}}. \tag{2.4.75}$$

The last term in (2.4.75) represents a low pass built by electrical parasitics of the laser, which were described in the previous sections. This low pass is characterized by its cut-off frequency f_p.

The modulation transfer function (2.4.75) has three parameters: the relaxation resonance frequency f_R, the damping factor γ and the cut-off frequency of electrical parasitics f_p. Accordingly, there are three types of limitations for the high speed operation of a semiconductor laser.

The first limitation is caused by the thermal effects, in fact by the internal laser heating, leading to an increase of the temperature of the active region. This is the so-called thermal limitation. Because temperature affects nearly each of the laser parameters used in the rate equations, the relaxation resonance frequency saturates at some current and starts to decrease at larger currents. Looking at (2.4.70) one can say, that the D-factor and the threshold current are temperature dependent, and the D-factor decreases with temperature, while the threshold current increases. Thus there is a limit for the relaxation resonance frequency, and it becomes limited by some maximum value $f_{R,\max}$. The maximum bandwidth that can be achieved in this case, assuming negligible damping and electrical parasitics, is

$$f_{-3\text{dB,thermal}} \approx \sqrt{1+\sqrt{2}}\cdot f_{R,\max} \approx 1.55\cdot f_{R,\max}. \tag{2.4.76}$$

The second limitation is the damping limit, also called internal limitation. It arises from the fact, that the damping factor increases with the squared relaxation resonance frequency (2.4.65), while the bandwidth increases only approximately linear to it. Starting from some point, increase in the damping factor overcomes the increase in the relaxation resonance frequency, and the bandwidth of the laser

begins to decrease. The maximum bandwidth possible in this case, assuming negligible electrical parasitics, is determined by the K-factor (2.4.67) and is

$$f_{-3\mathrm{dB,dampingl}} = \sqrt{2}\frac{2\pi}{K} \approx \frac{8.89}{K}. \tag{2.4.77}$$

The third type of limitations is caused by the presence of electrical parasitic elements inside of the laser, mostly parasitic resistances and capacitances. These electrical parasitics build a low pass, preventing high speed operation. With a given cut-off frequency of electrical parasitics f_p, maximum achievable bandwidth for an otherwise ideal case of perfect matching between relaxation resonance frequency and damping can be written down as

$$f_{-3\mathrm{dB,parasitics}} = \left(2+\sqrt{3}\right) f_p \approx 3.73 \cdot f_p. \tag{2.4.78}$$

The main goal of a researcher designing high speed VCSELs is to overcome these limitations. Commonly there are two or even all three types of limitations, which prohibit high speed laser operation. Consequently, one must apply many different concepts and very often some compromises should be met. Additionally, practical requirements like laser reliability, scalable and straightforward growth, fabrication and testing processes etc. should be satisfied.

References

1. Chuang SL (2009) Physics of photonic devices. Wiley, Hoboken
2. Coldren LA, Corzine SW (1995) Diode lasers and photonic integrated circuits. Wiley, New York
3. Kapon E (1999) Semiconductor lasers. Academic Press, San Diego
4. Cheng J, Dutta NK (2000) Vertical-cavity surface-emitting lasers: technology and applications. Gordon and Breach Science Publishers, Amsterdam
5. Crosslight, Crosslight Software Inc., http://www.crosslight.com/
6. PICS3D: photonic integrated circuit simulator in 3D, product description, http://www.crosslight.com/products/pics3d_mini_brochure.pdf
7. Silvaco, Silvaco Inc., http://www.silvaco.com/
8. WIAS TeSCA, Weierstraß-Institut für Angewandte Analysis und Stochastik, http://www.wias-berlin.de/software/tesca/index.html.de
9. Streiff M, Witzig A, Pfeiffer M, Royo P, Fichtner W (2003) A comprehensive VCSEL device simulator. IEEE J Sel Top Quantum Electron 9(3):879–891
10. Hadley GR (1995) Effective index model for vertical-cavity surface-emitting lasers. Opt Lett 20:1483–1485
11. Wenzel H, Wünsche HJ (1997) The effective frequency method in the analysis of vertical-cavity surface-emitting lasers. IEEE J Quantum Electron 33:1156–1162
12. Vukusic JA, Martinsson H, Gustavsson JS, Larsson A (2001) Numerical optimization of the single fundamental mode output from a surface modified vertical cavity surface emitting laser. IEEE J Quantum Electron 37:108–117
13. Klein B, Register LF, Hess K, Deppe DG, Deng Q (1998) Self-consistent Green's function approach to the analysis of dielectrically apertured vertical-cavity surface-emitting lasers. Appl Phys Lett 73(23):3324–3326

14. Noble MJ, Loehr JP, Lott JA (1998) Analysis of microcavity VCSEL lasing modes using a full-vector weighted index method. IEEE J Quantum Electron 34(10):1890–1903
15. Bienstman P, Baets R (2001) Optical modeling of photonic crystals and VCSEL's using eigenmode expansion and perfectly matched layers. Opt Quantum Electron 33(4/5):327–341
16. Bienstman P (2000–2001) Rigorous and efficient modelling of wavelength scale photonic components. Dissertation, Gent University, Faculty for Information Technologies, academic year 2000–2001
17. Bienstman P, Baets R, Vukusic J, Larsson A, Noble MJ, Brunner M, Gulden K, Debernardi P, Fratta L, Bava GP, Wenzel H, Klein B, Conradi O, Pregla R, Riyopoulos SA, Seurin J-FP, Chuang SL (2001) Comparison of optical VCSEL models on the simulation of oxide-confined devices. IEEE J Quantum Electron 37(12):1618–1631
18. CAMFR: Cavity Modelling Framework, http://camfr.sourceforge.net/
19. Itoh T (1989) Numerical techniques for microwave and millimeter-wave passive structures. Wiley, New York
20. Taflove A (1995) Computational electrodynamics, the finite-difference time-domain method. Artech House, Norwood
21. Morishita K (1983) Hybrid modes in circular cylindrical optical fibers. IEEE Trans Microw Theory Tech MTT-31(4):344–350
22. Ibanesen M, Johnson SG, Soljacic M, Joannopoulos JD, Fink Y, Weisberg O, Engness TD, Jacobs SA, Skorobogatiy M (2003) Analysis of mode structure in hollow dielectric waveguide fibers. Phys Rev E 67:046608
23. Aghaie KZ, Dangui V, Digonnet MJF, Fan S, Kino GS (2009) Classification of the core modes of hollow-core photonic-bandgap fibers. IEEE J Quantum Electron 45(9):1192–1200
24. Leisher PO, Chen C, Sulkin JD, Alias MSB, Sharif KAM, Choquette KD (2007) High modulation bandwidth implant-confined photonic crystal vertical-cavity surface-emitting lasers. IEEE Photonics Technol Lett 19(19):1541–1543
25. Danner AJ, Raftery JJ Jr, Leisher PO, Choquette KD (2006) Single mode photonic crystal vertical cavity lasers. Appl Phys Lett 88:091114
26. Song D-S, Kim S-H, Park H-G, Kim C-K, Lee Y-H (2002) Single-fundamental-mode photonic-crystal vertical-cavity surface-emitting lasers. Appl Phys Lett 80(21):3901–3903
27. Song D-S, Lee Y-J, Choi H-W, Lee Y-H (2003) Polarization-controlled, single-transverse-mode, photonic-crystal, vertical-cavity, surface-emitting lasers. Appl Phys Lett 82(19):3182–3184
28. Yang HPD, Chang YH, Lai FI, Yu HC, Hsu YJ, Lin G, Hsiao RS, Kuo HC, Wang SC, Chi JY (2005) Singlemode InAs quantum dot photonic crystal VCSELs. Electron Lett 41(20):1130–1132
29. Leisher PO, Danner AJ, Raftery JJ Jr, Siriani D, Choquette KD (2006) Loss and index guiding in single-mode proton-implanted holey vertical-cavity surface-emitting lasers. IEEE J Quantum Electron 42(10):1091–1096
30. Martinsson H, Vukusic JA, Grabherr M, Michalcik R, Jäger R, Ebeling KJ, Larsson A (1999) Transverse mode selection in large-area oxide-confined vertical-cavity surface-emitting lasers using a shallow surface relief. IEEE Photonics Technol Lett 11(12):1526–1538
31. Haglund A, Gustavsson JS, Vukusic J, Modh P, Larsson A (2004) Single fundamental-mode output power exceeding 6 mW from VCSELs with shallow surface relief. IEEE Photonics Technol Lett 16(2):368–370
32. Söderberg E, Gustavsson JS, Modh P, Larsson A, Zhang Z, Berggren J, Hammar M (2007) Suppression of higher order transverse and oxide modes in 1.3 μm InGaAs VCSELs by an inverted surface relief. IEEE Photonics Technol Lett 19(5):327–329
33. Mutig A (2004) Entwicklung von Oberflächenemittierenden Lasern. Diploma work, Technical University of Berlin, Institute of Solid State Physics, 3 May 2004
34. Stinavasan K, Borselli M, Painter O, Stintz A, Krishna S (2006) Cavity Q, mode volume, and lasing threshold in small diameter AlGaAs microdisks with embedded quantum dots. Opt Express 14(3):1094–1105
35. Piprek J (2003) Semiconductor optoelectronic devices. Elsevier Science, San Diego

36. Nextnano++, Walter Schottky Institut, Technische Universität München, Germany, http://www.wsi.tum.de/nextnanoplus/
37. Chang Y-C (2008) Engineering vertical-cavity surface-emitting lasers for high-speed operation. Dissertation, University of California, Santa Barbara, Dec 2008
38. Suzuki N, Anan T, Hatakeyama H, Fukatsu K, Tokutome K, Akagawa T, Tsuji M (2009) High speed 1.1 μm-range InGaAs-based VCSELs. IEICE Trans Electron E92-C(7):942–950
39. Al-Omari AN, Al-Kofahi IK, Lear K (2009) Fabrication, performance and parasitic parameter extraction of 850 nm high-speed vertical-cavity lasers. Semiconduct Sci Technol 24(9):095024 8 pp
40. Ou Y, Gustavsson JS, Westbergh P, Haglund A, Larsson A, Joel A (2009) Impedance characteristics and parasitic speed limitations of high speed 850 nm VCSELs. IEEE Photonics Technol Lett 21(24):1840–1842
41. Chang Y-C, Coldren LA (2009) Efficient, high-data-rate, tapered oxide-aperture vertical-cavity surface-emitting lasers. IEEE J Sel Top Quantum Electron 15(3):704–715
42. Hewlett-Packard Test and Measurement Application Note 95-1, S-parameter techniques for faster, more accurate network design, http://www.hp.com/go/tmappnotes, Hewlett-Packard Company, Palo Alto, CA, USA, 1997
43. Microwave Office, AWR, http://web.awrcorp.com/Usa/Products/Microwave-Office/
44. AppCAD, Avago Technologies, http://www.hp.woodshot.com/
45. TXLine, AWR, http://web.awrcorp.com/Usa/Products/Optional-Products/TX-Line/
46. Al-Omari AN, Carey GP, Hallstein S, Watson JP, Dang G, Lear KL (2006) Low thermal resistance high-speed top-emitting 980 nm VCSELs. IEEE Photonics Technol Lett 18(11):1225–1227
47. Satuby Y, Orenstein M (1999) Mode-coupling effects on small-signal modulation of multitransverse-mode vertical-cavity semiconductor lasers. IEEE J Quantum Electron 35(6): 944–954
48. Zei L-G, Ebers S, Kropp J-R, Petermann K (2001) Noise performance of multimode VCSELs. J Lightwave Technol 19(6):884–892
49. Westbergh P, Gustavsson JS, Haglund A, Sköld M, Joel A, Larsson A (2009) High-speed, low-current-density 850 nm VCSELs. IEEE JSTQE 15(3):694–703

http://www.springer.com/978-3-642-16569-6

High Speed VCSELs for Optical Interconnects

Mutig, A.

2011, XIV, 169 p., Hardcover
ISBN: 978-3-642-16569-6